Research Square

Preprints are preliminary reports that have not undergone peer review.
They should not be considered conclusive, used to inform clinical practice,
or referenced by the media as validated information.

Near-tip elastoplastic fracture mechanics of amorphous silica at small scale

Ayan Basu

Ayan.Basu@am.iitd.ac.in

Indian Institute of Technology Delhi

Gaurav Singh

Indian Institute of Technology Delhi

Research Article

Keywords: plasticity, EPFM, amorphous silica, J-integral, molecular statics

Posted Date: September 22nd, 2026

DOI: https://doi.org/10.21203/rs.3.rs-11081222/v1

License: This work is licensed under a Creative Commons Attribution 4.0 International License.
Read Full License

Additional Declarations: No competing interests reported.

Near-tip elastoplastic fracture mechanics of amorphous silica at small scale

Ayan Basu[1*] and Gaurav Singh[1]

[1]Department of Applied Mechanics, Indian Institute of Technology Delhi, New Delhi, 110016, India.

*Corresponding author(s). E-mail(s): ayan.basu@am.iitd.ac.in;
Contributing authors: gsingh@am.iitd.ac.in;

Abstract

Amorphous silica is widely used as an insulating layer in semiconductor and solar cell fabrication, where fracture behavior at the nanometer scale directly governs manufacturing precision and device reliability. Nanometer-scale exfoliation of amorphous silica requires a clear understanding of the crack growth mechanics. Fracture studies of amorphous silica have traditionally relied on linear elastic fracture mechanics. However, the recent establishment of plasticity near the crack tip at the atomistic scale calls for revisiting this assumption. In this present work, an elastoplastic fracture mechanics framework is utilized at the atomistic scale using molecular statics simulations. Local elastoplastic stress fields ahead of the crack tip are calculated from atomistic strain energy densities and finite strains at local atomistic sites. Further, a discretized, domain-integral formulation of the $\boldsymbol{J}$-integral is derived using a linear weight function. It has been demonstrated that even when the integral domain encloses the near-tip elastoplastic zone at the critical state just before crack propagation begins, the path independence of the critical $\boldsymbol{J}$-integral holds. The resulting critical $\boldsymbol{J}$-integral has been validated against multiple independent methods: a global energy release rate calculation, crack tip opening displacement estimates from both **90°** blunt-tip and direct methods. This fracture toughness has also been shown to translate to the continuum scale through an elastoplastic finite element analysis using the Ramberg-Osgood model. The methodology demonstrated in the present work is general in nature and maybe extended to any amorphous material.

Keywords: plasticity, EPFM, amorphous silica, $\boldsymbol{J}$-integral, molecular statics

1 Introduction

Amorphous silica, due to its low electric conductivity, large atomic band gap and chemical inertness, is widely used as an insulating material in various applications (Gupta (1985); Robertson (2006)). These properties, along with being a natural, non-toxic material, make silica one of the key insulating materials in semiconductor and renewable energy industries. In both solar cells and integrated circuit fabrication, layers of varying thicknesses are required for applications such as electrical and thermal insulation, light absorption, and more. In these applications, nanometer-thin layers of amorphous silica are necessary to achieve the performance efficiency required today. Thus, to achieve that precision, the mechanics of layer separation must be understood at the atomistic scale. A critical understanding of fracture mechanics at this scale would provide the necessary insight required to achieve such nanometer scale accuracy of the layer separation process required to fabricate efficient modern processors and solar cell insulators.

The elastic, fracture and failure of amorphous silica have been the subject of extensive research over the past several decades, both experimentally and computationally. Early experiments on silica glass have established Young's modulus and fracture energy (Marsh (1964); Wiederhorn (1969)). Their works generally support the linear elasticity theory while acknowledging the presence of plastic flow near the crack tip, primarily at elevated temperatures. Later, further research has also addressed the deformation mechanics of glass using a nonlinear elastic model (Gupta and Kurkjian (2005)); however, the problem of yielding remains unaddressed. Molecular statics and dynamics simulations have largely kept the linear elastic assumptions intact when describing the material. By utilizing BKS interatomic potential, researchers have found Young's modulus (somewhere equal and slightly higher compared to the experimental value of approximately 72 GPa (Wiederhorn (1969))) by just considering the initial region of the stress-strain diagram (van Beest et al. (1990); Muralidharan et al. (2006, 2007); Bansal and Doremus (2013)). Alternatively, the Vashishta potential has also been applied to study deformation mechanics, and it was found that an unconstrained (periodic in all three directions) ensemble produces a stress-strain diagram resembling that of a ductile material, compared to a small constrained ensemble, where brittle rupture was observed (Vashishta et al. (1990); Pedone et al. (2008)). More recently, the elastic moduli of amorphous silica were reported to be strain dependent, using ReaxFF (van Duin et al. (2003); Chowdhury et al. (2016)). The value of Young's modulus reported in this work (Chowdhury et al. (2016)) at lower strain rates was shown to be in agreement with the experimental results, the sharp increase of Young's modulus (338 GPa) at higher strain rates ($1.0 \times 10^{13} - 1.0 \times 10^{15}$ /s) was not addressed. From these earlier studies, researchers were able to justify the linear elastic assumptions for amorphous silica under small deformations. Similarly, linear elasticity was considered a sufficiently good approximation for solving mechanical problems involving amorphous silica.

The fracture and failure criteria for amorphous silica have been studied; however, most studies are based on the assumption that linear elastic fracture mechanics (LEFM) is valid. One of the earliest experimental works was done on micrometer thin silica films of 20 μm thickness and 500 μm length and varying width (between 60 and

140 μm) (Hatty et al. (2008)). The researchers created notches at the edge of varying lengths, between 3.5 and 15.5 μm, with a notch ratio of 0.9. 260 such specimens were tested under a uniaxial tensile test, and the maximum tensile load before failure was noted. The reported fracture toughness results showed a range of K_{IC} values in between 0.52 and 1.02 MPa$\sqrt{\text{m}}$, with an average value of the critical stress intensity factor reported as 0.81 $\pm$ 0.06 MPa$\sqrt{\text{m}}$. Although this earlier work presents a comprehensive report on the fracture toughness of amorphous silica, it does not justify the applicability of LEFM. An alternative experimental approach through way Vicker's indentation test has also been constructed (Bruns et al. (2020)). Following this methodology, researchers have done an extensive study on the fracture toughness of silica glass and silica nanopillars. In the case of glass panels, they have utilized a diamond micro-indenter to produce cracks along the corners of the indent. Although permanent deformation is responsible for creating the crack, the authors assumed that LEFM was valid ahead of the crack tip. This assumption was applied to silica surfaces with varying indent depths between 1 and 5 μm and the critical SIF was reported as 0.68 MPa$\sqrt{\text{m}}$.

Extensive molecular scale studies have also been conducted on the crack propagation initiation and growth of crystalline and amorphous silica. In an earlier study (Jones et al. (2018)), continuum balance laws and classical fracture mechanics theories were applied to molecular dynamics results to determine the fracture toughness of amorphous silica. An atomistic model of circular silica glass with a slit crack under mode-I tensile loading was studied. The Tersoff (Munetoh et al. (2007)) interatomic potential function was employed, and the model was maintained around 0 K temperature utilizing a Nosé-Hoover thermostat (Evans and Holian (1985)) (under an NVT environment). The K_{IC} value of the silica glass was reported to be much higher ($\approx$ 2.5 MPa$\sqrt{\text{m}}$) than the established experimental value ($\approx$ 0.81 MPa$\sqrt{\text{m}}$ (Hatty et al. (2008))). The researchers hypothesized that this discrepancy occurs because the bond breaking mechanism in amorphous silica is highly complex, meaning it cannot be adequately represented by the simple expression of the three-body Tersoff interatomic potential. Furthermore, it was noted that the stress profile ahead of the crack tip is complex and might not be completely elastic; therefore, the LEFM assumptions may not be valid.

The propagation of naturally occurring cracks in amorphous silica has also been investigated at the atomistic scale (Hao and Hossain (2019)). The formation and propagation of naturally occurring cracks in uncracked samples were studied alongside those in edge-cracked specimens. A key observation made by the researchers was that naturally occurring nanocracks consistently propagate at stresses beyond the yield strength of amorphous silica. However, in the presence of an existing pre-crack, the material fails before global yield strength is reached. Furthermore, for edge pre-cracked specimens with a crack length below 5 nm, the global stress required to initiate crack propagation exceeds the yield strength. The researchers have utilized Irwin's formula, $K_{IC} = \sigma_{\max}\sqrt{\pi a_0} f(a_0/w)$, as the linear elastic crack propagation initiation parameter. The fracture toughness value for crack propagation initiation was reported to be 1.32 MPa$\sqrt{\text{m}}$, which is slightly higher than the experimental value. This observation calls

into question the validity of LEFM and motivates the investigation of local stress components to better understand the problem.

A study of local stress and strain calculations near the crack tip was also conducted (Singh and Singh (2023)). There, the researchers have reported size independence by studying the variation of Young's modulus and Poisson's ratio for ensemble sizes ranging from 9600 to 115200 atoms. Under NPT conditions, using the BKS interatomic potential function, they provide a stress-strain diagram at various strain rates that cannot be considered a strictly linear elastic, brittle response. Nevertheless, LEFM was assumed to hold. However, in contrast to previous studies, they thoroughly studied the near-tip mechanics. There, the near-tip strain was calculated using atomistic deformation, and from there (using the elasticity tensor) stress components were measured. The researchers reported that the near-tip calculated stress intensity factor was 0.832 MPa$\sqrt{\text{m}}$. Although this result is comparable to earlier studies, the researchers have noted that the R^2 fit of the LEFM relation is not as high as it was for crystalline materials. This motivates to investigate if LEFM is valid near the crack tip.

The primary reason linear elasticity is insufficient is that researchers in recent years have observed that silica exhibits yielding and subsequent plasticity at the micro and nanoscale. Experimental and simulation studies on amorphous silica across various scales have consistently demonstrated yielding and plastic flow under both compressive and tensile loading (reporting yield strengths between 7.6 and 9 GPa) (Han et al. (2010); Yue and Zheng (2014); Wang et al. (2015); Kermouche et al. (2016)). From nanopillars and molecular-scale axial loading and volumetric compression, researchers have shown that the material's ductile response and yield strength are highly dependent on the strain rate (Ramachandramoorthy et al. (2019); Widmer et al. (2022)). While these studies successfully identify the onset of plasticity, yield plateaus, and general ductile characteristics, they lack detailed investigations into specific flow rules, shear-driven mechanisms, or the evolution of comprehensive elastoplastic parameters.

The existence of plasticity in amorphous silica has been firmly established in recent studies. Shear flow in this material was quantified under volumetric compression, demonstrating that post-yield material flow initiates gradually and generates large plastic shear under further loading—a phenomenon characterized as a "yield plateau" (Schill et al. (2018)). More recently, rigorous characterization of the small-scale plasticity of amorphous silica has been conducted at the atomistic scale (Basu and Singh (2026)). Utilizing molecular statics simulations, deformation data revealed that amorphous silica undergoes permanent plastic rearrangement beyond a yield stress of 9.55 GPa. Furthermore, evaluations of Drucker's inequalities across several discrete deformation states confirmed stable plastic hardening post-yielding, followed by perfect plasticity and, ultimately, softening prior to rupture. The yield and subsequent loading surfaces were also quantitatively shown to govern purely plastic deformation. In light of these findings regarding the elastoplastic nature of amorphous silica, elastoplastic fracture mechanics (EPFM) emerges as the necessary theoretical framework for evaluating critical fracture parameters. Consequently, the implementation of the J-integral and the analysis of its path dependence must be thoroughly considered.

Theoretically, the J-integral should be path independent irrespective of material and contour geometry. A detailed investigation of J-integral loops done on crystalline

silicon (Dutta and Singh (2024)) shows that with an increase in contour radius, the critical J-integral (J_C) changes only marginally. This earlier work indicates that a loop chosen very near the crack tip (about 5 Å) would provide a smaller J_C compared to larger loop radii. As the critical J-integral calculation procedure is material independent, this observation becomes very important for amorphous silica as well. Thus, the path independence of the atomistic scale J-integral calculation (though theoretically expected) is not generalized. The fundamental theories of continuum deformation were applied to develop an atomistic scale J-integral based on the Virial measure of stress (Rimsza et al. (2018)). There, the researchers conducted a molecular dynamics study of a 38,400 atom amorphous silica ensemble (density 2.187 g/cm^3) using the ReaxFF interatomic potential (van Duin et al. (2003)). During this analysis, the surface energy was calculated to obtain the critical J-integral. This work reported an enclosed plastic zone of about 20 Å ahead of the crack tip. The researchers have applied J-integral loops that are considered between 8 Å and 38 Å, and the critical stress intensity factor (K_{IC}) for the initiation of large-scale failures is about 2 MPa$\sqrt{\text{m}}$ for larger loops. Nevertheless, the average for all loops was reported to be 0.76 $\pm$ 0.16 MPa$\sqrt{\text{m}}$. The authors also provide calculations demonstrating the linear relationship between K_I^2 and J_I was valid up to the initiation of crack propagation. The authors conclude that J-integral provides more authentic results at atomistic scale simulation, and K_{IC} calculated near the crack tip was substantially higher than the K_{IC} values generally observed. These researchers hypothesized that the discrepancy is due to inelastic stresses ahead of the crack tip.

The study of J-integral based fracture criteria has been extended for a variety of ensemble sizes and crack lengths (Chowdhury et al. (2019)). Molecular dynamics studies were conducted on different silica ensembles ranging from 56,499 to 676,739 atoms, containing edge cracks with lengths ranging from 0.25 to 10 nm. The J-integral was considered as a measure of crack propagation initiation, utilizing a single counterclockwise square integration loop defined near the ensemble boundary. The researchers have reported that the critical J-integral values for crack propagation initiation (averaging 18.40 $\pm$ 0.10 J/m^2) are higher than experimental values and LEFM-based simulation data. This result reinforces the presence of inelastic stresses ahead of the crack tip. However, integration loops closer to the crack tip were not considered. Allowing the integration path to pass through the plastic zone would have been a more appropriate approach to address the plasticity ahead of the crack tip. Therefore, to better understand the phenomenon, elastoplastic stress calculations must be performed. A generalized elastoplastic fracture criterion is needed to accurately capture the mechanics ahead of the crack tip in the presence of plasticity.

As highlighted in the previously discussed atomistic studies, the presence of inelastic (elastoplastic) stress near the crack tip in amorphous silica limits the applicability of linear elastic fracture mechanics (LEFM). Therefore, to address the crack propagation initiation in a general manner, an elastoplastic fracture parameter is required. The critical J-integral (Rice and Rosengren (1968)) provides a rigorous, strain-energy-based measure for crack propagation criteria that is valid across linear elastic, nonlinear elastic, and elastoplastic materials. In the present work, Section 2 details the setup for the atomistic simulations and the subsequent recreation of the identical problem

in a finite element method (FEM) environment using the Ramberg-Osgood material model. Section 3 develops a discretized, atomistic-scale formulation of the critical J-integral for amorphous silica, which is validated against the critical energy release rate (ERR), the critical crack tip opening displacement (CTOD), and independent FEM calculations. Finally, Section 4 examines the accuracy of each method by comparing them with atomistically calculated critical J-integral values and validating the results against established experimental and simulation findings.

2 Simulation setup of mode-I fracture

2.1 Molecular statics simulation

For the present study, an ensemble of 1350000 atoms of amorphous silica has been selected, with dimensions 705.13 Å $\times$ 1632.85 Å $\times$ 17.60 Å. The specimen is created from β-crystalline silica using the quench melt (from 8000 K) rapid cooling method (Huff et al. (1999); Muralidharan et al. (2006)). The atomic masses assigned to silicon and oxygen are 28.0855 U and 15.9990 U, respectively. To obtain crack propagation initiation and growth in the atomistic silica ensemble, an embedded crack is created at the center of the $X_1 - X_2$ plane 1. The crack length is considered to be 235.04 Å (one third of the width), placed along the $X_1 - X_3$ plane at $X_2 = \frac{h}{2}$ with the crack tips directed along the X_1 direction. The ensemble and crack dimensions were strategically chosen to ensure that crack propagation initiates far from the loading, fixed, and idle side boundaries. This spatial isolation is necessary because the bulk fracture parameters have been shown to depend significantly on the distance from the loading boundary (Basu and Singh (2024)). Thus, without sufficient distance, the near-tip stress field would be influenced by external boundary effects rather than being governed exclusively by the crack alone. The crack itself is created by identifying the layers of atoms directly above and below the intended crack plane and switching off the atomic interactions between the atoms of these two layers, emulating the bond-breaking phenomena of an ideal slit crack.

To simulate this problem, the LAMMPS simulation tool is used (Thompson et al. (2022)) because it provides excellent scalability for such a large ensemble. The simulations employ the van Beest-Kramer-van Santen (BKS) interatomic potential to describe the atomic interactions in amorphous silica. The BKS potential has been extensively validated for reproducing the mechanical response of silica, including Young's modulus (Muralidharan et al. (2005); Silva et al. (2006); Yuan and Huang (2012); Singh and Singh (2023); Basu and Singh (2026)), yielding behavior (Wang et al. (2015); Schill et al. (2018); Basu and Singh (2026)), and critical stress-intensity factors (Rimsza et al. (2018); Singh and Singh (2023)). Importantly, for the present fracture simulations, the BKS potential has also been shown to reproduce the non-homogeneous stress field that develops ahead of a crack tip (Singh and Singh (2023); Basu and Singh (2026)), making it suitable for fracture mechanics. Although the BKS potential does not explicitly replicate bond-order terms, its functional form permits Si-O interactions to rearrange during deformation and therefore allows bond breaking and reconstruction without imposing a prescribed bond structure (Zhu et al. (2003)). In particular, the potential permits changes in Si-O coordination and the associated

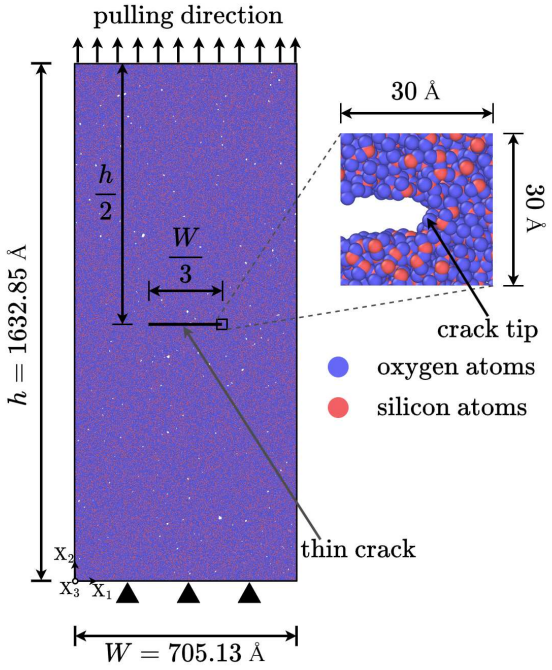


Fig. 1: Embedded crack model of amorphous silica.

redistribution of bond lengths and bond angles, thereby accommodating permanent structural rearrangements such as densification, defect formation, and local atomic reorganization (Mantisi et al. (2012); Yuan and Huang (2014)). These features are particularly relevant to crack-tip deformation, where the non-homogeneous stress field is bound to introduce local structural rearrangements even when far-field stresses remain within the yield limit. Thus, the BKS potential provides an appropriate atomistic description for the present study, in which both the crack-tip stress field and the bond breaking ahead of the crack tip are considered.

The boundary conditions in the X_1 and X_2 directions are considered shrink-wrapped, which means that the box size dynamically shifts to fit the atoms in both X_1 and X_2 directions, as shown in Figure 1. Furthermore, in the X_3 direction, the boundary condition is prescribed as periodic, so the plane-strain approximation in the quasi-continuum formulation is valid. The ensemble is initially equilibrated under NPT conditions at 1 K for 15 ps (15,000 steps) utilizing an iteration timestep of 0.001 ps. Following equilibration, the upper loading boundary is displaced at a constant rate to emulate a strain rate of 10^{-3} /ps while the lower boundary remains fixed. The subsequent deformation is simulated under an NVE ensemble at approximately 1 K, employing a Nosé-Hoover thermostat for 130 ps. Atomic positions, virial stress components, energy, and entropy are recorded at 5 ps intervals, while overall stress-strain data are recorded every 2 ps. Following the completion of the simulation, the

open-source visualization tool OVITO (Stukowski (2009)) is utilized to observe the initiation of crack propagation. The critical state of crack propagation initiation is defined as the state immediately preceding the initial observation of new bond breakage. As illustrated in Figure 2, this critical state occurs at $t = 60$ ps for the present ensemble, with crack propagation subsequently initiating at $t = 65$ ps. It is important to note that all deformation, strain, and stress components discussed in the present work are derived from the deformation at the critical state observed at $t = 60$ ps. The strain and stress calculation methodology is outlined in the following subsection.

2.1.1 Local stress and strain calculations

To accurately characterize the deformation ahead of a crack tip (at the identified critical state) where non-homogeneous strain and stress fields exist (Landes et al. (1979)), a robust calculation of local finite strain is required. This is achieved by employing a deformation gradient approach that maps material points from their initial equilibrium position $\boldsymbol{X}$ to their current deformed position $\boldsymbol{\chi}$ (Singh et al. (2014)). For amorphous silica, a linear mapping function

$$\chi_i = a_{ij} X_j + b_i \quad \text{where } i = 1, 2, 3 \tag{1}$$

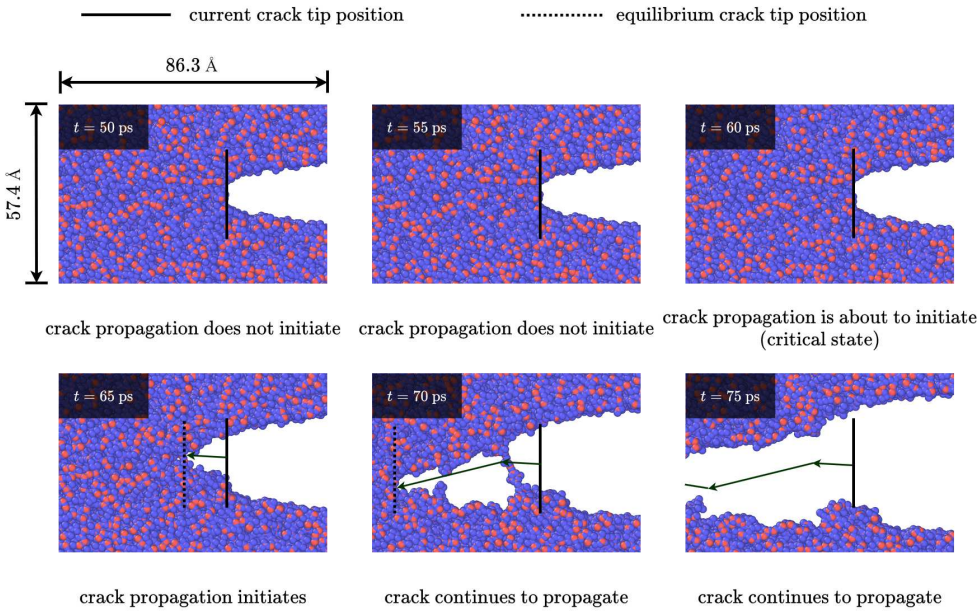
is considered, where a_{ij} and b_i are the unknowns to be determined. The linear deformation mapping function has been shown to be sufficient to characterize the near-tip strain field at for both crystalline and amorphous materials (Singh et al. (2014); Singh and Singh (2023); Basu and Singh (2026)). From this, mapping, the deformation gradient

$$F_{ij} = \frac{\partial \chi_i}{\partial X_j} = a_{ij} \tag{2}$$

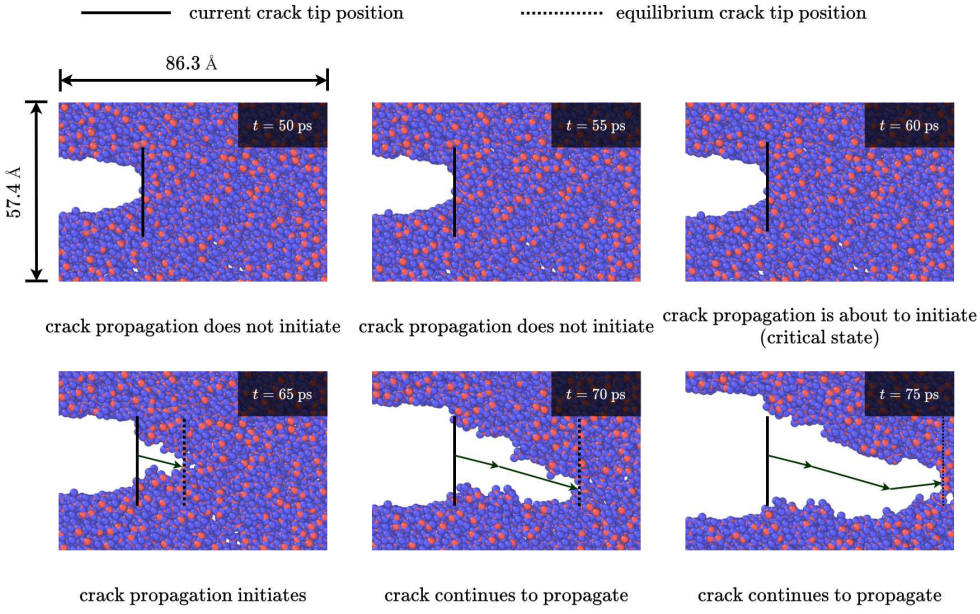
is extracted at each atomistic site ahead of the crack tip at the critical state, thus allowing for the calculation of the finite Lagrange strain as

$$\varepsilon_{ij} = \frac{1}{2}(F_{ki} F_{kj} - \delta_{ij}). \tag{3}$$

This linear deformation mapping remains highly effective even in the non-homogeneous strain field directly ahead of a crack tip at the critical state of crack propagation (Basu and Singh (2026)). However, the accuracy of this formulation relies heavily on the appropriate selection of the homogenization zone over which the mapping (Equation (1)) is to apply. Determining the mapping coefficients requires defining a local neighborhood of atoms, and the size of this homogenization zone dictates the accuracy of the calculated strain field. If this zone is chosen to be too large, the localized and non-homogeneous deformation features of the crack tip will be artificially averaged out, leading to a loss of local phenomena and an underestimation of peak strain components. Similarly, the zone cannot be chosen to be arbitrarily small due to mathematical constraints: in three dimensions, the linear mapping in Equation (1) introduces 12 unknowns (9 for the deformation gradient tensor a_{ij} and 3 for the translation vector b_i). Since each atom within the zone provides a set of three directional



(a) Left crack tip



(b) Right crack tip

Fig. 2: Atomistic view of near-tip deformation states during crack propagation initiation for an embedded crack. The initial and current crack tip positions are indicated by black dotted and solid vertical lines, respectively, while the arrows trace the path of crack propagation (after Basu and Singh (2026)).

equations corresponding to its spatial coordinates, a strict minimum of 4 atoms must be included in the homogenization zone to yield a determined system. Nevertheless, for reliable calculation, especially in amorphous materials like silica, where the local atomic arrangement varies, a slightly overdetermined system solved by optimization is recommended. Consequently, the homogenization zone must encompass at least 5 atoms. This also ensures that the calculated strain is not disproportionately skewed by the extreme or irregular displacement of any single atom, thereby preserving both the reliability of the tensor formulation and the accuracy required near the crack tip. This is demonstrated in Figure 3.

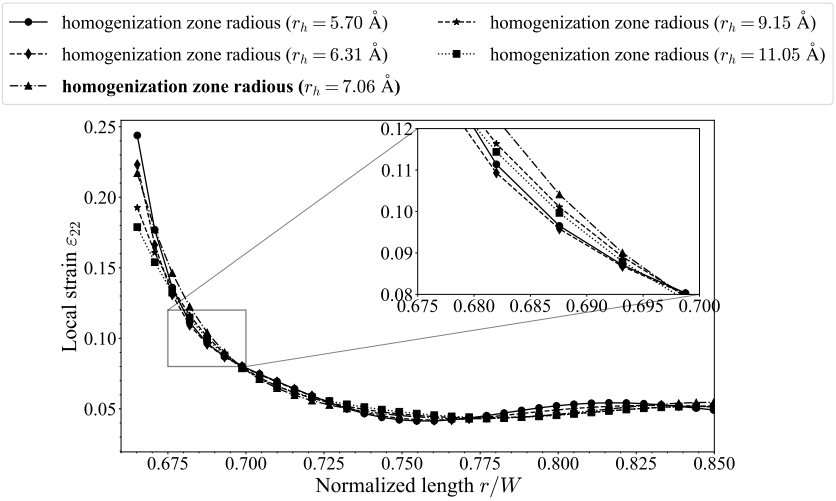


Fig. 3: 22-component of finite strain field ahead of the crack tip at the critical state of crack propagation initiation (the bold case indicates the considered homogenization for the present study).

As amorphous silica experiences yielding and plastic deformation (more so in the near-tip region), calculating the local elastoplastic stress is necessary, as the standard elastic assumption ($\sigma_{ij} = c_{ijkl}\varepsilon_{kl}$) becomes invalid (Lubliner (2008)). Thus, the inelastic stress components are obtained from the strain energy at each atomistic site. The starting point for relating atomistic energies to a continuum stress measure is the Gibbs free energy of the system, which in its full differential form is written as (Aragones et al. (2012); Liu (2024))

$$\mathrm{d}G = \mathrm{d}U + P\,\mathrm{d}V + V\,\mathrm{d}P - T\,\mathrm{d}S - S\,\mathrm{d}T, \tag{4}$$

where G is the Gibbs free energy of the system, U is the internal energy, P is the pressure, V is the volume, T is the absolute temperature, and S is the entropy. In Equation (4), the term $P\,\mathrm{d}V$ represents the work associated with a volumetric change under constant pressure, $V\,\mathrm{d}P$ represents the contribution from a change in pressure

at constant volume, $T\,\mathrm{d}S$ is the reversible heat exchanged due to a change in entropy, and $S\,\mathrm{d}T$ accounts for the entropy contribution arising from a temperature change.

In molecular statics (MS) simulations performed at approximately 1 K, a few simplifications follow directly from the simulation conditions. First, as $T \to 0\,\mathrm{K}$, and the thermostat setup ensures $\mathrm{d}T \approx 0\,\mathrm{K}$ during simulation, so the entropic terms $T\,\mathrm{d}S$ and $S\,\mathrm{d}T$ in Equation (4) can be ignored. Second, because the simulations are performed under volume conservation within an NVE ensemble, $\mathrm{d}V = 0$, eliminating the $P\,\mathrm{d}V$ term. Finally, the $V\,\mathrm{d}P$ contribution is consistently on the order of 10^{-4} relative to the potential energy and is therefore considered negligible. Under these conditions, Equation (4) reduces to

$$\Delta G \approx \Delta U. \tag{5}$$

Since the kinetic contribution to the total energy is likewise negligible at $T = 1\,\mathrm{K}$, the change in total energy of an atom is approximately equal to its change in strain (internal) energy (Horstemeyer and Baskes (1999); Lu et al. (2011)) as

$$\Delta E \approx \Delta U. \tag{6}$$

In a quasi-continuum framework, this strain energy density can be utilized to obtain the components of the elastoplastic stress tensor σ_{ij} through

$$\frac{\Delta U}{V_{ch}} = \int \sigma_{ij}\,\mathrm{d}\varepsilon_{ij}, \tag{7}$$

where $V_{ch} = \frac{4}{3}\pi r_{ch}^3$ is the characteristic volume of a local material point of radius r_{ch}, containing n atoms. For a local material point under plane strain approximation ($\varepsilon_{13} = \varepsilon_{23} = \varepsilon_{33} = 0$), the localized elastoplastic stress is extracted by solving the discrete form of the energy balance

$$\frac{1}{\frac{4}{3}\pi r_{ch}^3} \sum_{i=1}^{n} \Delta U_i = \frac{1}{2}\left(\sigma_{11}\varepsilon_{11} + 2\sigma_{12}\varepsilon_{12} + \sigma_{22}\varepsilon_{22}\right), \tag{8}$$

where ΔU_i is the change in strain energy of i^{th} atom, and σ_{11}, σ_{22}, σ_{12} and ε_{11}, ε_{22}, ε_{12} are the in-plane components of the local stress and strain tensors, respectively.

As shown in the comparison in Figure 4, this energy-based approach effectively captures the localized inelastic stress field directly ahead of the crack tip.

2.2 Finite element simulation

To validate the atomistic fracture simulation against a continuum benchmark, a finite element (FE) model of the same cracked geometry is analyzed in ABAQUS (Smith (2009)) under an elastoplastic constitutive assumption. Since the molecular statics stress field (shown in the red line in Figure 4) ahead of the crack tip is governed directly by the interatomic potential rather than by any assumed continuum constitutive law, it is treated as a reference solution against which the FE predictions (from the elastoplastic constitutive model) can be validated.

It has been recently established that amorphous silica demonstrates elastoplastic behavior at the small scale (Basu and Singh (2026)). This implies that an elastoplastic

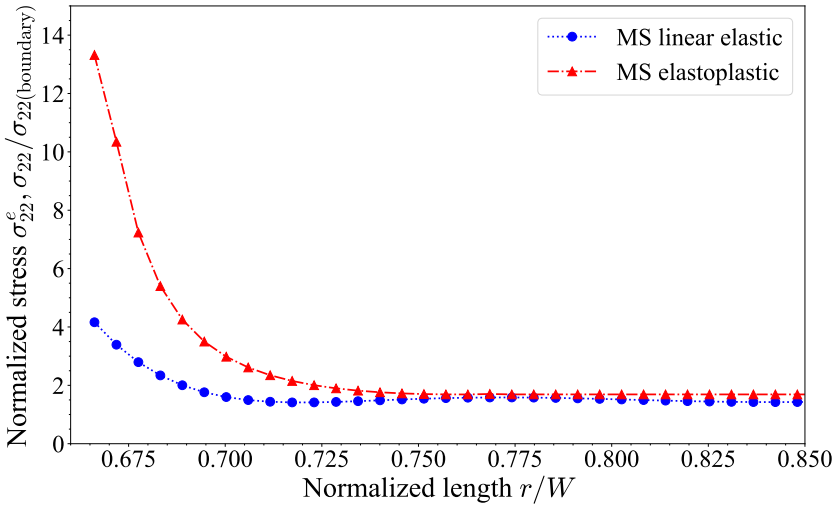


Fig. 4: Atomistically obtained normalized 22-component of elastic and elastoplastic stress ahead of the crack tip at the critical state of crack propagation initiation (after Basu and Singh (2026)).

constitutive model may be employed to conduct the FE simulation. The elastoplastic response is represented in ABAQUS using the Deformation Plasticity material model, which implements a Ramberg–Osgood elastoplastic material model of the following form (Ramberg and Osgood (1943); Smith (2009); Gadamchetty et al. (2016); Patwardhan et al. (2019))

$$E\boldsymbol{\varepsilon} = \boldsymbol{\sigma} + \alpha_0 \left(\frac{|\boldsymbol{\sigma}|}{\sigma_y}\right)^{(N-1)} \quad \text{or} \quad E\boldsymbol{\varepsilon} = \boldsymbol{\sigma} + \left(\frac{\alpha}{\sigma_y}\right)\left(\frac{\boldsymbol{\sigma}}{\sigma_y}\right)^{N} \tag{9}$$

where E is the Young's modulus, σ_y is the yield strength, α is the constant and N is the exponent of Ramberg-Osgood elastoplastic model. The generalized formulation is extended to three-dimensional stress states by employing the generalized Hooke's law for the linear elastic response, and utilizing a von Mises equivalent stress with an associated flow rule beyond local yielding (Metzger et al. (2015))

$$E\,\boldsymbol{\varepsilon} = (1+\nu)\,\mathbf{S} - (1-2\nu)\,p\,\mathbf{I} + \frac{3}{2}\left(\frac{\alpha}{\sigma_y}\right)\left(\frac{q}{\sigma_y}\right)^{N}\mathbf{S}, \tag{10}$$

where $\boldsymbol{\varepsilon}$ is the finite strain tensor, $\boldsymbol{\sigma}$ is the resulting elastoplastic stress tensor, ν is the Poisson's ratio, $\mathbf{S}$ is the stress deviator, defined as

$$\mathbf{S} = \boldsymbol{\sigma} + p\,\mathbf{I}, \tag{11}$$

p is the equivalent hydrostatic stress defined as

$$p = -\frac{1}{3}\boldsymbol{\sigma} : \mathbf{I}, \tag{12}$$

and finally q is the Mises equivalent stress defined as

$$q = \sqrt{\frac{3}{2}\mathbf{S} : \mathbf{S}}. \tag{13}$$

To apply this material model for amorphous silica, the required material constants are listed in Table 1 below with the values taken from the work of Basu and Singh (2026).

Table 1: Material properties of amorphous silica.

Property	Symbol	Value
Young's modulus	E	75.26 GPa
Poisson's ratio	ν	0.22
yield strength	σ_y	9.55 GPa
Strain at which Yield occurs	ε_y	0.13850
Ramberg-Osgood model constant	α_0	4.63
Ramberg-Osgood model exponent	N	13.25

As shown in Figure 5, the finite element geometry is taken exactly as the molecular statics specimen dimensions (shown in Figure 1). A thin embedded slit crack of width 23.13 nm (one-third of the specimen width) is placed at the mid-plane, as shown schematically in the figure.

The crack is designated in ABAQUS using the Contour Integral crack definition. A seam is first introduced along the crack faces so that the two faces are geometrically on the same coordinates but kinematically independent (as shown in Figure 6a), allowing them to separate under load. The crack is modeled explicitly by assigning duplicate nodes on the crack faces, with zero traction imposed along the crack faces. The crack tip is represented by a single node, with a refined mesh in the near-tip region (Figure 6b). The crack front is then specified as a single node, and the crack extension direction, q vector (as shown in Figure 6a), is defined normal to the crack front and in the plane of crack growth. Around the crack tip, a denser mesh of collapsed quadrilateral elements is used; for a non-hardening or plastically deforming tip, the collapsed elements are given non-singular behavior, and quadratic shape functions are employed for this setup (as shown in Figure 6b).

The Contour Integral is then specified, with four sub-contours in between the red and the black circles shown in Figure 6a (region highlighted in light blue) to confirm domain independence of the computed stress field. This is further used as the comparison with the atomistically computed elastoplastic stress field shown in

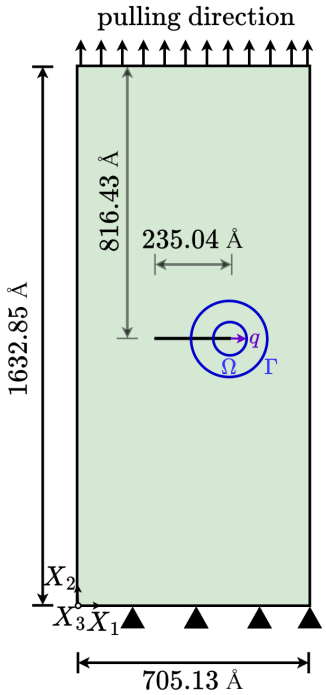


Fig. 5: FE model of amorphous silica with an embedded crack.

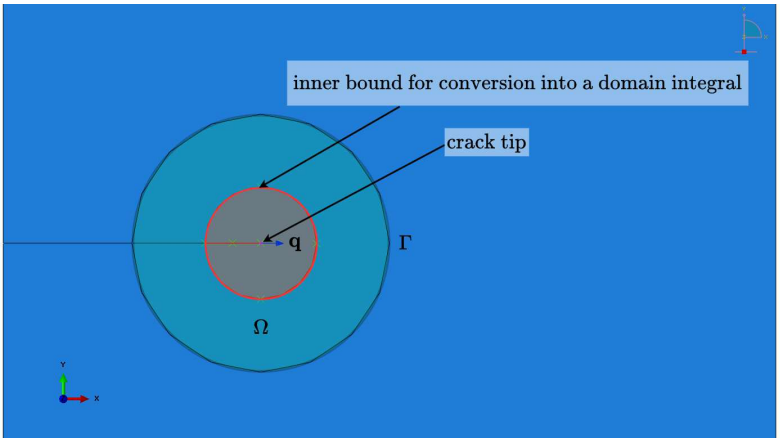
Figure 4. The boundary-value problem is constructed from the equilibrium (strong-form) equation

$$\nabla \cdot \boldsymbol{\sigma} + \mathbf{b} = \mathbf{0} \quad \text{in } \Omega \tag{14}$$

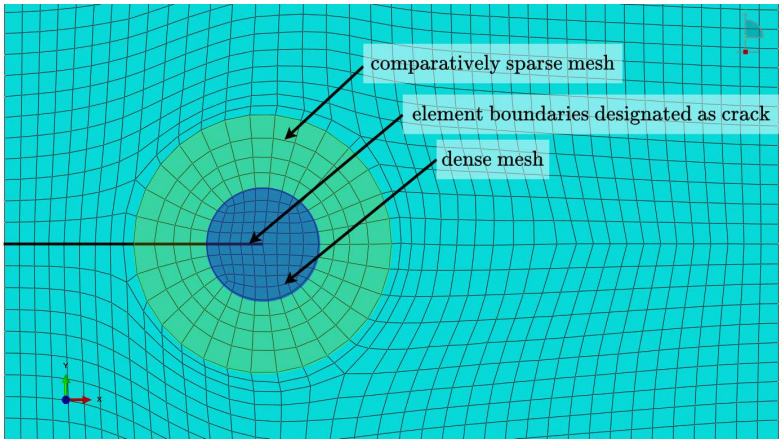
400 subject to the traction and displacement boundary conditions

$$\begin{aligned} \boldsymbol{u} &= \bar{\boldsymbol{u}} \quad \text{on } \Gamma_u, \\ \boldsymbol{\sigma}\boldsymbol{n} &= \bar{\boldsymbol{t}} \quad \text{on } \Gamma_t, \\ \boldsymbol{\sigma}\boldsymbol{n} &= \bar{\boldsymbol{t}}_c = \mathbf{0} \quad \text{on } \Gamma_c \end{aligned} \tag{15}$$

where $\boldsymbol{\sigma}$ is the Cauchy stress tensor obeying the deformation plasticity constitutive law detailed above (in Equations (9)-(13)), $\mathbf{b}$ is the body force density assumed to be negligible. Moreover, Γ_c is the traction-free crack faces. In the present study, the applied displacement on the boundary Γ_u is taken as zero to impose a fixed boundary
405 condition. Furthermore, $\bar{\boldsymbol{t}}$ is taken as the critical boundary stress required for the crack propagation initiation. From the molecular statics simulation, $\bar{\boldsymbol{t}}$ is observed to be 3.868 GPa (calculated at $t = 60$ ps at the atomistic scale) at the loading boundary.



(a) Schematic of the domain-integral formulation for J-integral evaluation, where the contour Γ around the crack tip is transformed into an equivalent domain Ω, and $\mathbf{q}$ denotes the virtual crack-extension direction used in ABAQUS.



(b) Near-tip discretization for the EPFM analysis, showing the designated crack and refined mesh near the crack tip (characteristic length 2.25) compared to the far-field (characteristic length 4.9) for the 22,745-element model.

Fig. 6: Near-tip mesh discretization and the corresponding domain-integral formulation used for J-integral evaluation in the elastic-plastic fracture mechanics (EPFM) analysis.

The weak form of the problem is obtained to be

$$\int_{\Omega} \nabla^s \boldsymbol{v} : \boldsymbol{\sigma}(\boldsymbol{u})\, \mathrm{d}\Omega = \int_{\Omega} \boldsymbol{v} \cdot \boldsymbol{b}\, \mathrm{d}\Omega + \int_{\Gamma_t} \boldsymbol{v} \cdot \bar{\boldsymbol{t}}\, \mathrm{d}\Gamma_t + \underbrace{\int_{\Gamma_c} \boldsymbol{v} \cdot \bar{\boldsymbol{t}}_c\, \mathrm{d}\Gamma_c}_{=0 \text{ (traction-free crack surface)}} \tag{16}$$

where the strain field is computed using the Green–Lagrange strain measure, retaining the nonlinear displacement-gradient contribution so as to be directly analogous to the finite-deformation strain calculation employed in the molecular statics framework

$$\nabla^s \boldsymbol{u} = \frac{1}{2}\left(\nabla \boldsymbol{u} + (\nabla \boldsymbol{u})^T + (\nabla \boldsymbol{u})^T \nabla \boldsymbol{u}\right) = \boldsymbol{\varepsilon}(\boldsymbol{u}), \tag{17}$$

where $\boldsymbol{\varepsilon}(\boldsymbol{u})$ is the resulting strain tensor associated with the displacement field $\boldsymbol{u}$. Consistent with this strain definition, the term $\nabla^s \boldsymbol{v} : \boldsymbol{\sigma}(\boldsymbol{u})$ is the virtual work density generated by a variation $\boldsymbol{v}$ and the resultant Cauchy stress $\boldsymbol{\sigma}(\boldsymbol{u})$ at any material point of the body and used in the weak-form equilibrium equation solved by the finite element method. Solving this problem provided us with the stress field ahead of the crack tip as shown in Figure 7. The 22-component of the stress field ahead of the crack

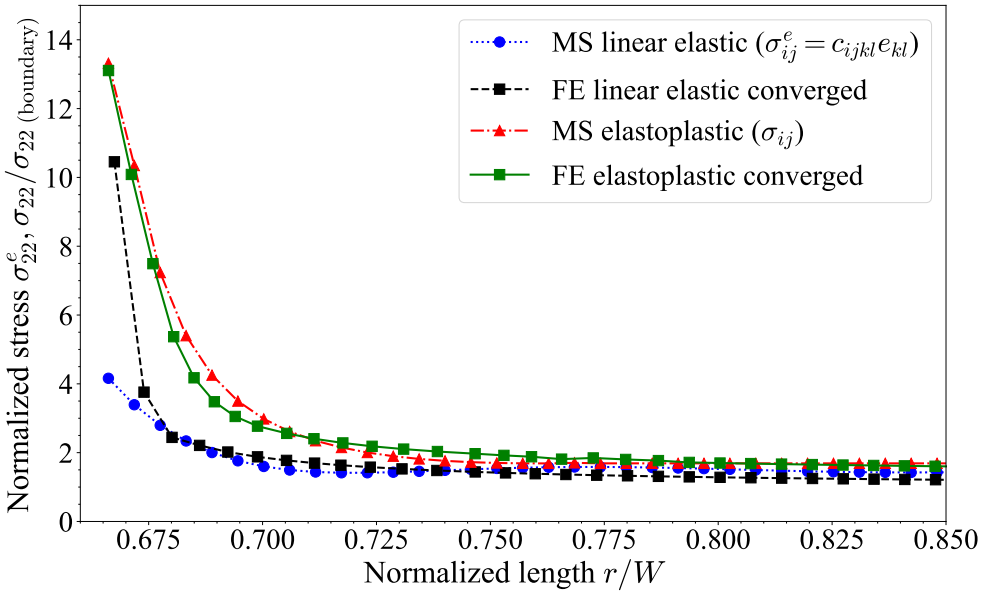


Fig. 7: Normalized 22-component of elastoplastic stress ahead of the crack tip at the critical state of crack propagation initiation as established (after Basu and Singh (2026)).

tip, normalized by the corresponding boundary stress $\sigma_{22\,(\text{boundary})} = 3.868$ GPa, is

compared across the linear elastic and elastoplastic solutions in Figure 7. Both the molecular statics (MS) calculation and finite element (FE) elastoplastic predictions show substantially higher stress values near the crack tip when compared to the solutions obtained under the assumptions of linear elasticity (highlighted in blue dotted line for MS and black dashed line for FE in Figure 7). This deviation marks the presence of plastic deformation near the crack tip, within which crack propagation initiation can no longer be characterized by the stress intensity factor. The difference between the linear elastic and elastoplastic solutions in the near-tip region reflects a breakdown of the small-scale yielding assumption and therefore cannot be neglected. This limits the applicability of linear elastic fracture mechanics (LEFM) in accurately describing crack initiation and growth in amorphous silica. Notably, the elastoplastic FE predictions converge towards the MS elastoplastic solution as the mesh is refined, supporting the finite element discretization adopted for the elastoplastic analysis. Taken together, these observations strongly motivate the adoption of an elastoplastic fracture mechanics (EPFM) framework, in which the initiation and subsequent growth of cracks are governed by energy-based or path-independent parameters, such as the energy release rate or the J-integral, which inherently account for the accompanying plastic deformation. The following section develops this elastoplastic fracture mechanics framework for amorphous silica.

3 Elastoplastic fracture mechanics of amorphous silica

The presence of elastoplastic stress near the crack tip in amorphous silica implies that LEFM near the crack tip can no longer be applied. Thus, to address crack propagation initiation, a more general fracture parameter is required. The J-integral, originally proposed by Rice (Rice and Rosengren (1968)), provides a rigorous, strain-energy-based measure of crack-propagation criteria that is valid for all kinds of linear or nonlinear elastic and elastoplastic materials. The line integral is defined as

$$J = \int_{\Gamma} \left(U \mathrm{d}y - \boldsymbol{T} \frac{\partial \boldsymbol{u}}{\partial x} \mathrm{d}\Gamma \right) \tag{18}$$

where Γ is a continuous contour surrounding the crack tip from one crack face to the other. The traction vector $\boldsymbol{T}$ is defined along the outward normal of the contour with components $T_i = \sigma_{ij} n_j$, and U is the strain energy density given as $U = \int_0^{\varepsilon} \sigma_{ij} \mathrm{d}\varepsilon_{ij}$. The J-integral is mathematically path-independent, provided the contour does not cross a non-homogeneous boundary (Rice and Rosengren (1968); Khan and Biswas (2010); Zhang et al. (2025)). Since the strain energy of each atom near the crack tip has already been determined (as detailed in Section 2.1.1), the critical J-integral (J_C) can directly be computed at the onset of crack propagation.

At the atomistic scale, the classical definition of line contour becomes inapplicable due to the absence of continuous stress and strain fields, as it is almost impossible to ensure a continuous array of atomistic sites along any given contour. This holds true for amorphous solids like silica as well. Thus, in these discrete systems, the line integral has to be converted to a three-dimensional domain, inside which sufficient atomistic sites can be ensured for a reasonable calculation. Such a discretized or domain-based formulation of the J-integral has been widely applied to crystalline (Dutta and Singh

(2025); Jia et al. (2022); Khare et al. (2007); Gucci et al. (2025)) and amorphous materials (Sohail and Roy (2023)). In the following subsection, the formulation of the discrete volumetric J-integral will be expressed in terms of the local stress, strain, energy density, and displacement at each atomistic site. It is important to note that the formulation preserves the essential path-independent character of the J-integral while enabling direct computation of the J-integral from atomistic calculations.

3.1 Discretized J-integral using the loop method

As established in the above discussion, application of the J-integral at the atomistic scale Equation (18) is to be converted into a discrete sum over a set of atomistic sites. To derive such an expression, the J-integral is first written as a continuous integral in indicial notation as

$$J = \int_\Gamma \left(U \, \mathrm{d}X_2 - T_i \frac{\partial u_i}{\partial X_1} \, \mathrm{d}\Gamma \right) = \int_\Gamma \left(U \, \mathrm{d}X_2 - \sigma_{ij} n_j u_{i,1} \, \mathrm{d}\Gamma \right). \tag{19}$$

where n_j denotes the in-plane outward unit normal components to the infinitesimal contour segment $\mathrm{d}\Gamma$ (as shown in Figure 8), which allows the coordinate derivatives $(\mathrm{d}X_i)$ to be expressed as

$$\begin{aligned} \mathrm{d}X_1 &= n_2 \, \mathrm{d}\Gamma \\ \mathrm{d}X_2 &= n_1 \, \mathrm{d}\Gamma. \end{aligned} \tag{20}$$

Applying the above in the first part of Equation (19), the following can be obtained

$$\int_\Gamma U \mathrm{d}X_2 = \int_\Gamma U n_1 \mathrm{d}\Gamma = \int_\Gamma U \delta_{1j} n_j \mathrm{d}\Gamma, \tag{21}$$

and putting this back in Equation (19) the entire J-integral can now be expressed in terms of $\mathrm{d}\Gamma$ as

$$J = \int_\Gamma \left(U \delta_{1j} n_j - \sigma_{ij} u_{i,1} n_j \right) \mathbf{d}\Gamma = \int_\Gamma \left(U \delta_{1j} - \sigma_{ij} u_{i,1} \right) n_j \mathrm{d}\Gamma. \tag{22}$$

This expression of the J-integral is commonly used as an alternative representation in simulation studies, as it is easier to compute numerically (Dutta and Singh (2024); Khare et al. (2007); Jia et al. (2022); Stenström and Eriksson (2021)). However, in its current form, this formulation remains inapplicable to discrete atomistic domains. Specifically, in an amorphous system of atoms, the structural disorder does not permit a reliable calculation of the line contour, rendering direct evaluation of a line integral infeasible. To resolve this, the line integral is to be converted into an equivalent area integral. This area integral can then be extended across the system's thickness to define a three-dimensional volumetric domain, allowing strains, displacements, stresses, and strain energies to be evaluated via discrete summation over the enclosed atoms.

To convert the line integral derived in Equation (22) into an area integral, the Gauss divergence theorem has to be applied. Similar to Figure 8, the calculation of the

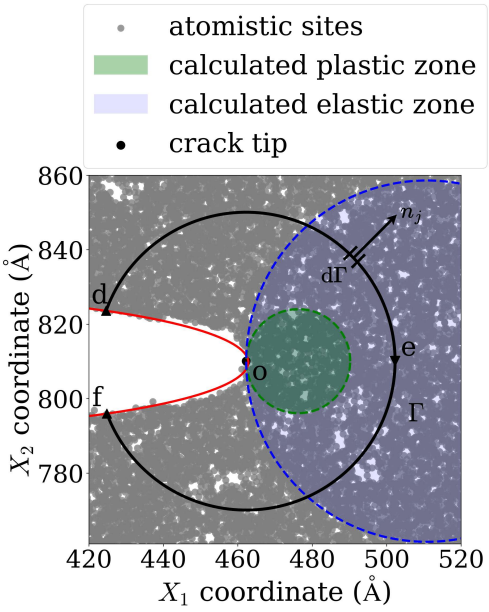


Fig. 8: Local atomistic view in the vicinity of the crack tip with calculated plastic zone radius $r_p = 27.94$ Å at the critical state of crack propagation showing the line for J-integral calculation (atomistic sites are represented as smaller gray points and do not represent their actual size).

J-integral in the surface domain requires a well-defined domain where the divergence theorem is to be applied. Figure (9) represents the critical state of crack propagation initiation (at $t = 60$ ps) of a mode-I fracture simulation (shown in the Figure 2a and 2b).

The crack faces and near-tip geometry at the critical state are modeled using an elliptical surface representation. This choice is physically appropriate for embedded cracks (Watanabe (2020)), whereas edge cracks have been modeled using parabolic functions (Dutta and Singh (2025)). Using the atomic coordinates of the crack surface, the elliptical representation of the crack opening profile is calculated as

$$\frac{(X_1 - 349.9050)^2}{112.9007^2} + \frac{(X_2 - 809.7827)^2}{18.4301^2} = 1 \tag{23}$$

which corresponds to the red curve in Figure 9. This ellipse provides a geometric approximation of the crack faces and serves as the reference boundary for defining the integration domain of the J-integral.

The domain Ω_J to be used for the area integral evaluation of the J-integral on the X_1–X_2 plane is defined by two concentric contours around the crack tip. The inner contour Γ_i (radius r_1) is bounded by the curve 'abc', and the outer contour Γ_o (radius r_2) is bounded by the curve 'def' as can be seen in Figure 9. The region enclosed by

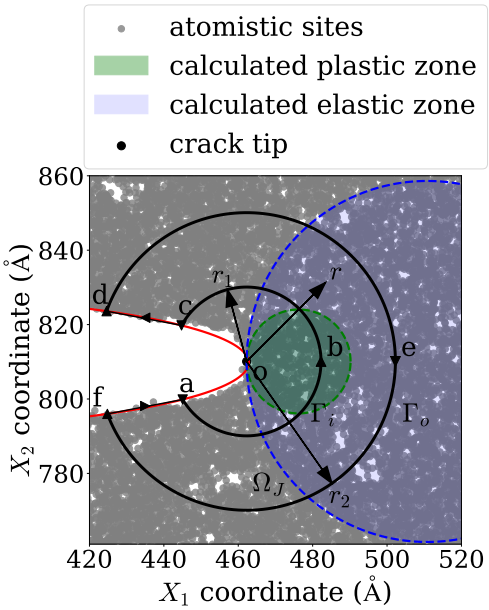


Fig. 9: Local atomistic view in the vicinity of the crack tip at the critical state of crack propagation showing the domain Ω_J for J-integral calculation (atomistic sites are represented as smaller gray points and do not represent their actual size)

the elliptical crack surface and these two contours forms the closed path 'abcdefa'. This bounded region allows for the application of the divergence theorem.

Moreover, the green shaded region in Figure 9 identifies the plastic zone ahead of the crack tip, which is governed by inelastic deformation. In contrast, the blue shaded region denotes the K-dominated linear elastic zone. Provided that both Γ_i and Γ_o completely encompass the crack tip and the inelastic zone, the radii r_1 and r_2 can be selected arbitrarily. Under these conditions, the computed J-integral should be theoretically path-independent and independent of the specific contour area. This will also be verified at a later stage of the present study.

While the J-integral could theoretically be obtained through a direct discrete summation of Equation (22) over all atomistic sites, a smooth scalar weight function q is widely adopted to ensure integration domain independence (Dutta and Singh (2024); Jia et al. (2022); Stenström and Eriksson (2021); Okada and Ohata (2013); Nikishkov et al. (2016)). This smooth scalar field transforms the traditional line integral into an equivalent area (or volume) integral by attaching weight to each integrand point, analogous to the Gauss weight function widely used in numerical integrals. In this context, q serves as a local scaling factor that determines the contribution of each atomistic site to the overall sum (which will be derived below). The function is prescribed such that $q = 1$ on the inner contour ($r = r_1$, curve 'abc') and $q = 0$ on the outer contour ($r = r_2$, curve 'def'). The advantage of this weighted approach is its numerical stability, as the discrete summation of the integrand remains invariant in this case, even

if the number of atomistic sites within the domain changes significantly as the inner and outer radii are widely varied.

Various approaches exist for defining the weight function in fracture mechanics. While some studies employ higher-order functions in Cartesian coordinates ($q \equiv q(X_1, X_2)$) (Jia et al. (2022); Nikishkov et al. (2016)), they do not substantially improve the accuracy of the results (Jia et al. (2022)). Consequently, a simpler, linearly decreasing radial function has often been utilized (Dutta and Singh (2025); Jia et al. (2022); Okada and Ohata (2013)). Thus, the present study adopts a linear weight function expressed as

$$q = \frac{r - r_1}{r_2 - r_1} \tag{24}$$

where r_1 and r_2 are already defined and r is the radial distance of the given atomistic site inside the domain Ω_J. Now, multiplying Equation (24) to the integrand of Equation (22) gives

$$J = \int_\Gamma \left(U\delta_{1j} - \sigma_{ij}u_{i,1}\right) n_j q \mathrm{d}\Gamma. \tag{25}$$

For simplicity of calculation, a part of the integrand is defined as

$$F_j \overset{\text{def}}{=} \left(U\delta_{1j} - \sigma_{ij}u_{i,1}\right) q. \tag{26}$$

Now, the application of the divergence theorem on the above equation yields

$$J = \int_\Gamma \left(U\delta_{1j} - \sigma_{ij}u_{i,1}\right) n_j q \mathrm{d}\Gamma = \int_\Gamma F_j n_j \mathrm{d}\Gamma = \int_{\Omega_J} \frac{\partial F_j}{\partial X_j} \mathrm{d}A \tag{27}$$

where $\mathrm{d}A$ is the infinitesimal area element on the domain Ω_J. For further discretization steps, $\frac{\partial F_j}{\partial X_j}$ has to be expanded as

$$\frac{\partial F_j}{\partial X_j} = \left(U\delta_{1j} - \sigma_{ij}u_{i,1}\right) \frac{\partial q}{\partial X_j} + q \left\{ \frac{\partial}{\partial X_j} \left(U\delta_{1j} - \sigma_{ij}u_{i,1}\right) \right\}. \tag{28}$$

After simplification (shown in Appendix A), the above expression yields

$$\frac{\partial F_j}{\partial X_j} = \left(U\delta_{1j} - \sigma_{ij}u_{i,1}\right) \frac{\partial q}{\partial X_j}. \tag{29}$$

Thus, the final form of the converted area integral (Equation (27)), using the divergence theorem is

$$J = \int_{\Omega_J} \left(U\delta_{1j} - \sigma_{ij}u_{i,1}\right) \frac{\partial q}{\partial X_j} \mathrm{d}A. \tag{30}$$

Finally, the discretized form of the integral is obtained by summing the integrand over all atomistic sites within the domain Ω_J across the thickness of the ensemble,

which can be expressed as

$$J = \sum_{\alpha=1}^{N} \left[\left(U A_0 \delta_{1j} - \sigma_{ij} A_0 u_{i,1} \right) \frac{\partial q}{\partial X_j} \right]_\alpha \tag{31}$$

where U is the calculated strain energy at a given atomistic site, σ_{ij} is the calculated elastoplastic stress calculated using the method outlined in Section 2.1.1 and A_0 is the average area occupied by an atomistic site. The average area is calculated under the assumption that an atomistic site is homogeneous with radius 'r_{ch}', thus the area is calculated as $A_0 = \frac{V_{ch}}{t}$, where V_{ch} is the accumulative volume occupied by the atomistic site ($V_{ch} = \frac{4}{3}\pi r_{ch}^3$) and t is the average thickness occupied by the atomistic site (calculated by dividing total thickness by the number of atomistic sites throughout the thickness). Furthermore, as the linear mapping (as shown in Equation (1)) is considered for the finite strain calculation, u_i can be written as

$$u_i = \chi_i - X_i = a_{ij} X_j + b_j - X_i = a_{ij} X_j + b_j - \delta_{ij} X_j = (a_{ij} - \delta_{ij}) X_j + b_j. \tag{32}$$

Re-writing $u_{i,1}$ of Equation (31) as

$$\frac{\partial u_i}{\partial X_1} = (a_{ij} - \delta_{ij}) \frac{\partial X_j}{\partial X_1} = (a_{ij} - \delta_{ij}) \delta_{j1}. \tag{33}$$

Therefore, the only remaining unknown to solve the discrete sum in Equation (31) is the derivative of the weight function q. As the linear wave function of the form of Equation (24) is taken for the present work, the derivative (derivation given in Appendix B) is considered to be

$$\frac{\partial q}{\partial X_j} = \frac{1}{r(r_2 - r_1)} \begin{bmatrix} X_1 \\ X_2 \end{bmatrix} \tag{34}$$

where X_1 and X_2 denote the positional components of an atomistic site. An in-house Python code was developed to evaluate the discrete J-integral summation (Equation (31)) at the critical state of crack propagation initiation in amorphous silica. The J-integral is theoretically path-independent (Rice and Rosengren (1968)). The discrete formulation is therefore expected to show the same behavior. To verify this, contour loops with varying inner and outer radii were utilized.

Table 2 shows results for a fixed inner radius $r_1 = 20$ Å, with the outer radius r_2 increased from 30 Å to 70 Å. The critical J-integral, J_C^{MD}, is taken as the average of these values and is found to be 119.9980 GPa-Å. Similar calculations for r_1 ranging from 10 Å to 40 Å are given in Appendix C and yield identical results.

The plastic zone radius is calculated as $r_p = 27.94$ Å (shown in Figure 8). All contours in this study, therefore, enclose both the elastoplastic zone and the outer K-dominated elastic field. This confirms that the reported J_C is a valid, locally measured fracture parameter. Across all nine contours in Table 2, J ranges from 111.45 to 131.60 GPa-Å, with a standard deviation of about 6.9 GPa–Å (∼5.8% of the mean).

Table 2: Discrete J-integral values and percentage deviation with respect to the first contour ($r_2 = 30$ Å).

r_1 (Å)	r_2 (Å)	No. of atoms in domain (N)	$r_2 - r_1$ (Å)	J (GPa-Å)	% deviation
20	**30**	**1578**	**10**	**116.4319**	**0.00**
20	35	2567	15	115.3477	−0.93
20	40	3760	20	125.1045	+7.45
20	45	5141	25	111.4472	−4.28
20	50	6755	30	113.4899	−2.53
20	55	8499	35	131.6031	+13.03
20	60	10383	40	129.2669	+11.02
20	65	12530	45	122.6145	+5.30
20	70	14671	50	114.6764	−1.51
				$J_C = 119.9980$	

The largest deviations are attributed to local fluctuations, since J returns to within a reasonable limit when averaged. This scatter is expected in atomistic domains and does not indicate path dependence. Table 3 shows J_C for r_1 between 10 and 40 Å. Deviations stay within ±3% of the reference value at $r_1 = 20$ Å. J_C increases mildly from $r_1 = 10$ Å to $r_1 = 35$ Å, then drops back at $r_1 = 40$ Å. This confirms that once $r_2 - r_1 \geq 10$ Å, the choice of inner contour has a negligible effect on J_C.

Table 3: Dependence of the critical J-integral on the inner contour radius r_1.

r_1 (Å)	Critical J-integral (J_C) (GPa-Å)	% deviation w.r.t. J_C at $r_1 = 20$ Å
10	117.7726	−1.85
15	119.3063	−0.58
20	**119.9980**	**0.00**
25	121.4678	+1.22
30	122.3379	+1.95
35	123.4148	+2.85
40	119.4629	−0.45

Based on these evaluations, the critical atomistic J-integral is taken as

$$J_C^{\mathrm{MS}} = 119.9980 \text{ GPa} - \text{Å}. \tag{35}$$

where the superscript MS indicates this calculation os obtained from direct molecular statics simulation.

A rigorous quantitative validation of this calculated value against established literature will be presented in subsequent sections. Together, these confirm the path independence of the computed J-integral, which holds once $r_1 \geq 20$ Å and $r_2 - r_1 \geq 10$ Å. This independence agrees with prior work on crystalline materials (Dutta and Singh (2025)) (path independence for $r_1 \geq 10$ Å), 2D graphene (Roy and Roy (2019)),

and amorphous epoxy (Sohail and Roy (2023)). However, path independence alone does not confirm accuracy. The following subsections further verify J_C against the energy release rate (ERR) and crack-tip opening displacement (CTOD) using the relevant atomistic-scale theory.

3.2 Calculation of energy release rate (ERR)

The energy release rate (ERR) G depends on the total potential energy of the ensemble. It does not primarily reflect near-tip mechanics. Even so, it remains a useful quantity for characterizing the fracture mechanics of amorphous silica. Prior atomistic studies support this approach, offering some useful insights. In nickel crystals, ERR was estimated from crack surface energy and plastic work, but the critical ERR increased with model size (Xu and Demkowicz (2020)). This size-dependence is not theoretically consistent, since a true critical ERR should be a size-independent material property. A similar energy-balance method was used for brittle fracture in silicon (Swadener et al. (2002)). Studies have also established that ERR is size, strain-rate and crack length independent (Zhang et al. (2014)). In the present work, ERR is calculated as

$$G_C = -\frac{\mathrm{d}W}{\mathrm{d}A} \approx -\frac{\Delta W}{\Delta A} \tag{36}$$

where W is the total external work and ΔA is the new crack surface area created just after crack propagation begins (the immediate next state of the crack propagation initiation shown in Figure 2a). As observed in Figure 2a and Figure 2b, crack growth starts at the 65^{th} ps of the simulation. The change in crack length and potential energy is therefore taken between the 60^{th} ps (critical state, just before propagation begins) and the 65^{th} ps (Figure 10).

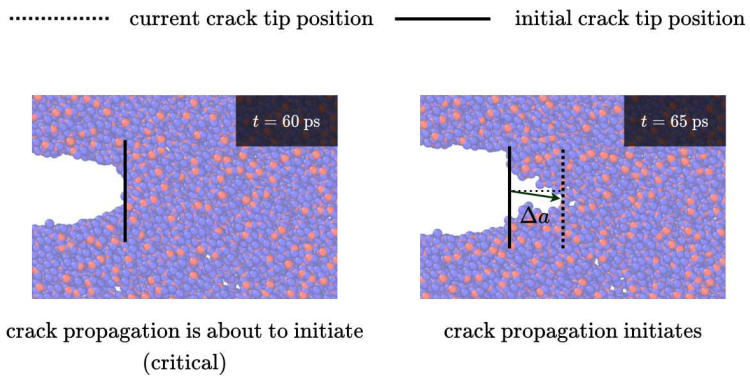


Fig. 10: Atomistic view of the critical state of crack propagation and the immediate next crack propagation state.

The change in external work is reflected directly in the change in potential energy from the MD simulation. The ensemble thickness t_s is constant at 17.610 Å. The discretized expression is therefore

$$G_C = \frac{U_{65} - U_{60}}{2t_s\,\Delta a} \tag{37}$$

where the factor 2 accounts for the two newly created crack surfaces. Using the potential energy change from the simulation, the critical ERR is

$$G_C^{\mathrm{MS}} = \frac{530399.8250 - 468108.4820}{2 \times 17.61 \times 15.60} = 113.7407 \text{ GPa-Å}. \tag{38}$$

This value is comparable to the critical J-integral calculated earlier, $J_C^{\mathrm{MS}} = 119.9980$ GPa-Å (the comparison is possible because $G = J$). This close agreement is consistent with fundamental fracture mechanics theory (Anderson (2017)), and supports the reliability of both independent calculations. However, G_C^{MS} is computed from the total work over the entire simulation ensemble, not from near-tip fields alone. Therefore, a near-tip cross-check is needed. This is given by the crack tip opening displacement CTOD–ERR relationship, which holds in both linear elastic and elastoplastic analysis.

CTOD can be measured at the atomistic scale using two methods:

- 90° blunt-tip method- treats the crack tip as a point and uses ±45° construction lines.
- Direct method- measures the separation between crack faces directly at the blunted tip.

Both methods are discussed below.

3.3 Calculation of critical J-integral from CTOD

3.3.1 90° blunt-tip method

In the 90° blunt-tip method, the crack tip opening displacement (CTOD) is defined using a geometric construction. This construction treats the crack tip as a sharp, point-like location. The first step is to identify the crack tip position (as shown with a black dot in Figure 11) and the orientation of the crack plane (as shown with a black solid line in Figure 11). This step is important as the entire geometric construction depends on these two reference crack planes. Once the crack tip and crack plane are defined, two straight lines are drawn from the crack tip. One line is inclined at +45° to the crack plane, and the other at −45°. Together, these lines form a right angle. The lines are extended outward until they intersect the crack faces. The +45° line intersects the upper crack face, and the −45° line intersects the lower crack face at two distinct points (shown with purple and yellow dots, respectively, in Figure 11). The CTOD is defined as the absolute distance between these two intersection points. This distance represents the effective crack opening near the tip.

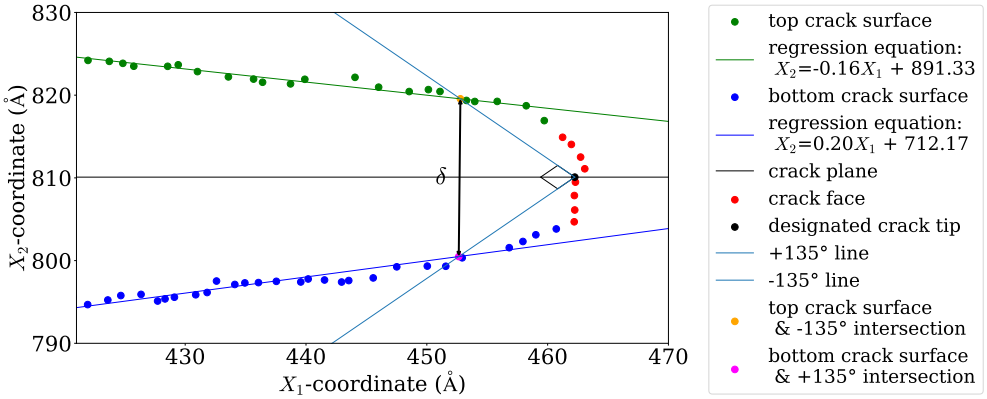


Fig. 11: CTOD measurement at the critical state just before crack propagation in the X_1-X_2 plane using linear fits to upper (green) and lower (blue) crack faces, and the intersections with $\pm 135°$ lines define the CTOD (black dashed line). The crack plane is located at $X_2 = 810.09$ Å.

A key advantage of this method is its behavior under crack tip blunting. The measurement lines are inclined away from the immediate crack tip. This makes the method less sensitive to local tip blunting. Even if plastic deformation or atomic rearrangement changes the exact tip geometry, the construction stays stable, as long as the crack tip position can still be reasonably defined. For this reason, the 90° blunt-tip method is widely used in both static (Zhu et al. (2017); Samadian et al. (2018); Nathan et al. (2021)) and fatigue (Zhu et al. (2017)) crack growth experiments. The same methods have also been applied in atomistic simulations of crystalline materials (Dutta and Singh (2025)). In this earlier work, the crack tip is identified from the atomic configuration, and the $\pm 45°$ lines are constructed within the simulation domain to compute the crack face separation. In this present work, the upper and lower crack faces are approximated as straight lines. These lines are obtained by linear least-squares regression on the atomic site coordinates of the top and bottom crack faces, as shown in Figure 11. Only sites sufficiently far from the crack tip are included in the regression. This avoids distortion caused by crack-tip blunting. Figure 11 shows the crack tip opening in the X_1-X_2 coordinate system. The upper crack face atomic sites, shown in green, are used to obtain the linear equation for the upper crack surface as

$$X_2 = -0.16X_1 + 891.33 \quad (R^2 = 90.09\%). \tag{39}$$

The lower crack face atomistic sites, shown in blue (in Figure 11), are used similarly to obtain the linear equation for the lower crack surface as

$$X_2 = 0.20X_1 + 712.17 \quad (R^2 = 93.25\%). \tag{40}$$

The crack plane (a line in this two-dimensional representation) corresponds to the X_1-X_3 plane located at $X_2 = 810.09$ Å (solid black line in Figure 11). The crack tip locus on the X_1-X_2 plane is taken at $(X_1 = 462.15,\ X_2 = 810.09)$ Å.

Now the CTOD itself is obtained from these reference lines, which is defined as the vertical separation between the two intersection points, highlighted by the dashed black line in Figure 12. This construction keeps the measurement away from the atomic-scale irregularities at the crack tip. The calculated value is $\delta_{90^\circ} = 19.07$ Å, as shown in Figure 12.

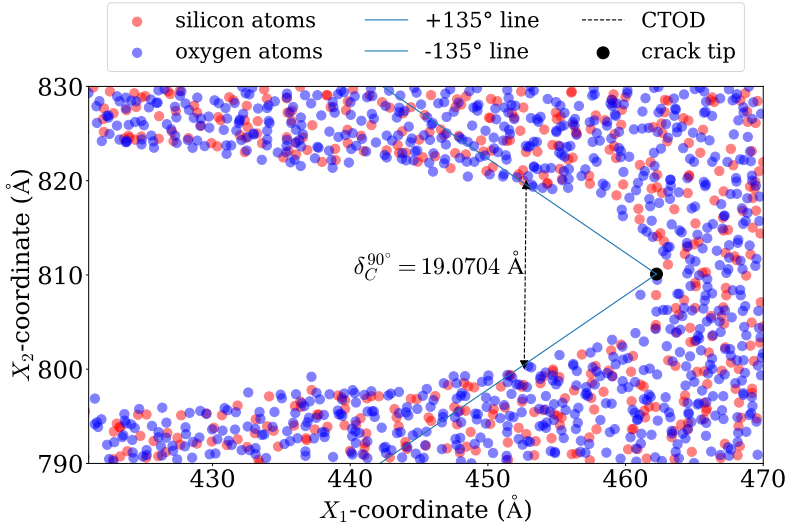


Fig. 12: Atomistic site positions at the critical state just before crack propagation, obtained from the 60 ps timestep of the molecular simulation. CTOD measurement uses the $\pm 45^\circ$ geometric construction in the X_1–X_2 plane; the dashed vertical line indicates $\delta_{90^\circ} = 19.0704$ Å.

This approach provides a stable definition of crack opening in atomistic simulations and remains consistent with the geometric principles of the 90° intercept method used in experimental fracture mechanics. With the CTOD now calculated, the following CTOD-ERR relationship can be used to obtain the critical energy release rate for amorphous silica as

$$G_C = \frac{\pi \delta \sigma_y}{4} \tag{41}$$

where σ_y is the yield strength.

For this present method, the energy release rate at the critical state is calculated as

$$G_C^{90^\circ} = \frac{\pi \delta_C^{90^\circ} \sigma_y}{4}. \tag{42}$$

The yield strength of amorphous silica is taken as $\sigma_y = 9.55$ GPa (Table 1). Substituting this value gives

$$G_C^{90^\circ} = 143.04 \text{ GPa-Å}. \tag{43}$$

This result can now be compared with the two earlier estimates of the fracture parameter. The critical J-integral was $J_C^{\text{MS}} = 119.9980$ GPa-Å, and the energy-balance ERR was $G_C^{\text{MS}} = 113.7407$ GPa-Å. The 90° blunt-tip estimate, $G_C^{90^\circ} = 143.04$ GPa-Å, is higher than both J_C^{MS} and G_C^{MS}.

3.3.2 Direct method

In the direct method, the CTOD is defined as the normal distance between the two crack faces near the crack tip. The normal separation is evaluated either at the crack tip or at a fixed distance behind it. The CTOD is obtained from the intersection points of the normal line to the crack plane with the upper and lower crack faces. This method can be applied in both atomistic and continuum frameworks. In atomistic models, a group of atoms is used to represent the blunt crack tip. In node-based continuum methods, a corresponding set of nodes serves the same purpose. The direct method is particularly suited to elastoplastic fracture problems (Anderson (2017)), where significant crack tip blunting occurs. Under such conditions, the original crack tip position cannot be uniquely defined, and the 90° blunt-tip method becomes difficult to apply.

The direct method is also difficult to apply in experimental techniques such as Digital Image Correlation (DIC), as very high speed and resolution are required for this experimental application (Ktari et al. (2014)). For this reason, it may be primarily applied in computational methods, where nodal or atomic positions are directly available and crack tip identification is possible. At the atomistic scale, this method has been used to calculate CTOD in crystalline aluminum (Velilla-díaz et al. (2021)) and silicon (Dutta and Singh (2025); Skogsrud and Thaulow (2015)). In these studies, atoms near the crack tip were selected to define the crack geometry and compute the opening displacement. A similar nodal-based implementation has also been used in finite element method (FEM) simulations, reported for FCC crystalline materials (Liu et al. (2011)) and structural steels (Chu and Liu (2014); Cui and Guo (2020)), where nodal displacements were used to evaluate crack-opening displacement using the same geometric definition.

In the present work, the direct method is applied at the atomistic scale, using the same linear representations of the upper and lower crack surfaces obtained from the crack-face regression analysis in the 90° blunt-tip method (as shown in Figure 11). Here, the crack tip is treated as a blunt surface, in contrast to the single point used in the 90° blunt-tip method. The crack tip location is instead identified from the near-tip atomistic configuration at the critical state of crack propagation. This is done by assigning the red atoms in Figure 11 to define the blunt tip. Based on these atoms, a vertical line is constructed normal to the crack surface in the X_1-X_2 plane, as shown in Figure 13.

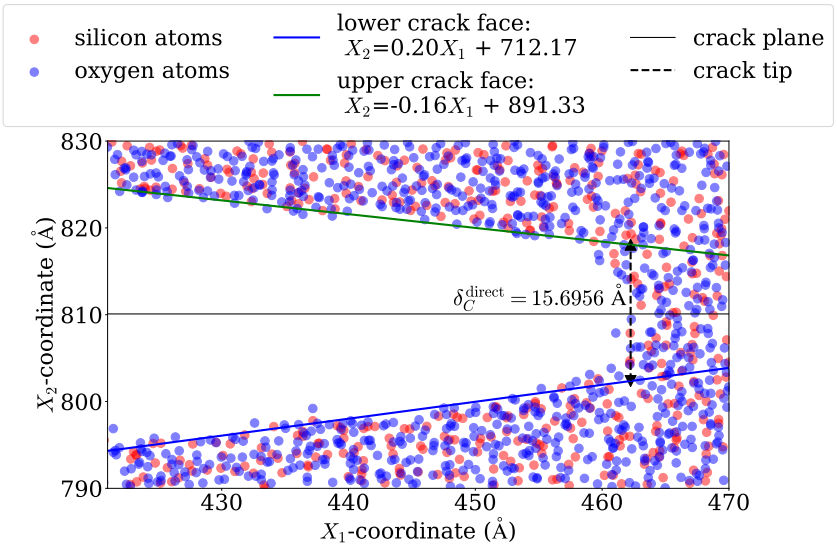


Fig. 13: Atomistic configuration at the critical state just before crack propagation, where the crack tip opening displacement is calculated directly at the crack tip, normal to the crack plane. The dashed vertical line represents the measured normal separation, $\delta_C^{\text{direct}} = 15.6956$ Å.

The intersection points between this normal line and the previously defined upper and lower crack-surface lines are found next. The CTOD is calculated as the normal distance between these two intersection points. This construction takes the measurement directly at the crack tip. As a result, it is sensitive to local blunting and atomic rearrangement at the critical state, as seen in Figure 13. The calculated value is $\delta_C^{\text{direct}} = 15.70$ Å. With the CTOD determined by the direct method, the CTOD-ERR relationship (Equation (41)) can again be invoked to estimate the critical energy release rate. For the direct method, this is expressed as

$$G_C^{\text{direct}} = \frac{\pi \delta_C^{\text{direct}} \sigma_y}{4} = 117.73 \text{ GPa-Å}. \tag{44}$$

The critical J-integral and the corresponding ERR have now been evaluated using several independent approaches: the direct MD contour-loop method, direct energy release rate and two CTOD-based formulations. The 90° blunt-tip method gives $G_C^{90^\circ} = 143.04$ GPa-Å, in contrast, the direct method gives $G_C^{\text{direct}} = 117.73$ GPa-Å, which is only 1.89% below J_C and 3.51% above G_C^{MS}. The direct method is therefore in much closer agreement with both J_C and G_C^{MS} than the 90° blunt-tip method.

This agreement is because the direct method measures CTOD directly at the blunted crack tip, capturing the same local near-tip mechanics that govern the J-integral. The 90° method, by contrast, measures CTOD away from the tip using a fixed geometric angle. This makes it less sensitive to the actual blunted geometry, and therefore less accurate under significant crack tip blunting (due to plasticity).

Since amorphous silica exhibits considerable blunting prior to propagation, the direct method is expected to be the more reliable here, and its closer agreement with both J_C^{MS} and G_C^{MS} reflects this observation.

Based on these atomistic evaluations of elastoplastic fracture parameters, the computed critical J-integral may be considered an atomistic scale crack initiation criterion. However, a complete and physically consistent interpretation requires that this critical value also be examined within a continuum framework and compared against continuum-scale predictions.

All atomistic evaluations presented so far are based on discrete, atomistic site observations. Such simulations become computationally expensive at larger length scales and different configurations. A continuum mechanics-based approach is therefore required to compute the J-integral under elastoplastic fracture conditions in a computationally efficient manner. For this purpose, the finite element method (FEM) is employed in the present work, using an elastoplastic constitutive model. The FEM simulation methodology has already been described in Section 2.2. In the following section, the J-integral results are discussed in detail.

3.4 J-integral from finite element analysis

Atomistic scale calculations of J-integral are based on a discrete sum of atomistic sites inside the domain. Such simulations become computationally expensive at larger length scales or complex geometries. Thus, a continuum-mechanics approach has to be setup as a complementary method used to calculate the J-integral for amorphous silica, using the finite element method (FEM) in ABAQUS. The same simulation methodology and geometric construction used for the near-tip elastoplastic stress measurement are adopted here, since this approach has already been shown to reproduce the appropriate elastoplastic stress distribution near the crack tip. These details are already discussed in Section 2.2 before.

In the context of quasi-static finite element fracture analysis, the J-integral is evaluated over a closed integration domain. The virtual crack extension method (Parks (1977)) is used here. This method is based on the fracture mechanics formulation of Shih, Moran, and Nakamura (Shih et al. (1986)). Within ABAQUS, the J-integral in two dimensions (plane strain) is defined as the limit of a contour integral enclosing the crack tip (Smith (2009)) as

$$J = \lim_{\Gamma \to 0} \int_{\Gamma} \mathbf{n} \cdot \mathbf{H} \cdot \bar{\mathbf{q}} \, \mathrm{d}\Gamma \tag{45}$$

where Γ is the integration contour, beginning on one crack face and ending on the opposite face. Here, $\bar{\mathbf{q}}$ is a unit vector in the local virtual crack extension direction, shown in Figure 6a and $\mathbf{n}$ is the outward normal to the contour (Parks (1977); Shih et al. (1986)). Furthermore, the tensor $\mathbf{H}$ is defined as

$$\mathbf{H} = W\mathbf{I} - \boldsymbol{\sigma} \frac{\partial \mathbf{u}}{\partial \mathbf{X}}, \tag{46}$$

where W is the strain energy density, $\boldsymbol{\sigma}$ is the Cauchy stress tensor, and $\mathbf{u}$ is the displacement field (Parks (1977); Shih et al. (1986)). For elastoplastic materials, W is taken as the sum of the elastic strain energy density and the plastic dissipation (Gurtin et al. (2013); Mase et al. (2020); Basu and Singh (2026)). The implementation of this formulation in finite element analysis is obtained by converting Equation (45) into an equivalent domain integral using the divergence theorem. This domain excludes the crack tip itself, which improves numerical stability and reduces mesh sensitivity, as shown in Figure 6a. In this implementation, several concentric contours are defined around the crack tip, and the J-integral is computed for each one. The number of sub-contours must be specified by the user. Thus, in this present work, for a properly refined mesh and a converged solution, the computed J-integral values should be path-independent across these contours. The obtained solution is therefore tested for both the number of sub-contours and the mesh size.

The mesh sensitivity of J-integral was carried out first, to confirm the convergence of the computed J-integral. The accuracy of the domain integral in Equation (45) depends strongly on discretization and element density near the crack tip. Bi-quadratic, 8-noded, plane-strain (CPE8R) elements are therefore used to discretize the domain. Three mesh sizes were considered: a fine mesh with 22745 elements, an intermediate mesh with 7214 elements, and a sparse mesh with 928 elements (same as the sizes utilized to obtain the stress profile shown in Figure 7). For each mesh, the light blue contour shown in Figure 6a is divided into four sub-contours for evaluation of the J-integral. Mesh independence is verified by checking for minimal variation among these contour values. The computed J-integral values for all three mesh densities are summarized in Table 4.

Table 4: J-integral mesh sensitivity study using the domain integral formulation in ABAQUS at the critical state just before crack propagation (EPFM with Ramberg-Osgood material model).

No. of Elements	**Contour 1** (GPa-Å)	**Contour 2** (GPa-Å)	**Contour 3** (GPa-Å)	**Contour 4** (GPa-Å)	**Average J-integral** (GPa-Å)
22,745	**120.20**	**120.40**	**120.50**	**120.70**	**120.45**
7214	119.60	119.90	120.10	120.30	119.98
928	119.40	119.20	120.00	120.80	119.85

The results presented in Table 4 demonstrate consistency in the computed J-integral values across all mesh sizes. The maximum deviation between the finest and most sparse mesh for the J-integral value is 0.60 GPa-Å, corresponding to a relative difference of approximately 0.50%. The computed J-integral is path-independent across the evaluated contours, confirming the validity of the domain-integral formulation and the crack-tip discretization. For the finest mesh, the maximum contour deviation is 0.50 GPa-Å. For the intermediate mesh, the maximum deviation is about 0.58%. The sparse mesh (928 elements) shows a maximum deviation of approximately

1.34%. From these results, it can be concluded that a finer mesh reduces variation in the J-integral calculation. Although the coarsest mesh shows a slightly larger overall deviation, the variation remains within an acceptable range for elastoplastic fracture analysis. Thus, in the present study, it can be concluded that the calculation of J-integration is independent of the mesh size.

Following the mesh sensitivity analysis, the finest mesh consisting of 22,745 elements was selected for further evaluation of contour dependence. To verify the path independence of the J-integral for the present problem, the number of contours was varied from 3 to 7, with all other simulation parameters held constant. As discussed earlier, ABAQUS evaluates the J-integral using a domain integral formulation. For a properly converged mesh and a stable nonlinear solution, the computed J-integral values should exhibit minimal variation with changes in the contour number. Therefore, this study provides further verification of the solution's numerical stability. The results of this contour sensitivity study are summarized in Table 5. Convergence is assessed by examining the variation of J-integral values across successive contours, together with the deviation of the average value. A stable, low-variation result across contours would also support the applicability of the Ramberg-Osgood elastoplastic model for computing the J-integral of amorphous silica.

The average for each simulation with varying contours is taken as the critical J-integral (for that given number of sub-contours) and reported in Figure 14. The sub-contour sensitivity results presented in Table 5 and Figure 14 further confirm the path independence of the domain integral for the refined mesh (consisting of 22745 elements). The variation of the J-integral across different sub-contours is observed to be negligible, further demonstrating the numerical stability of the solution and confirming sufficient crack-tip refinement under quasi-static elastoplastic fracture mechanics.

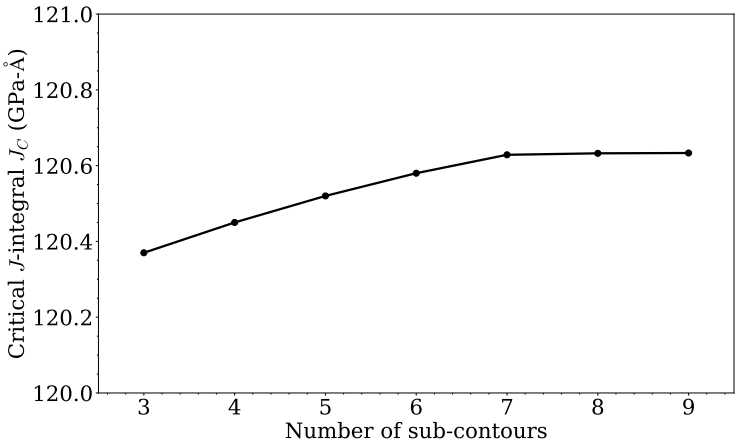


Fig. 14: Average J-integral values for varying number of contours using the finest mesh (22,745 elements)

Table 5: Contour sensitivity study of the J-integral at the critical state just before crack propagation using the finest mesh (22,745 elements).

No. of Contours	**Contour 1** (GPa-Å)	**Contour 2** (GPa-Å)	**Contour 3** (GPa-Å)	**Contour 4** (GPa-Å)	**Contour 5** (GPa-Å)	**Contour 6** (GPa-Å)	**Contour 7** (GPa-Å)	**Contour 8** (GPa-Å)	**Contour 9** (GPa-Å)
3	120.20	120.40	120.50	–	–	–	–	–	–
4	120.20	120.40	120.50	120.70	–	–	–	–	–
5	120.20	120.40	120.50	120.70	120.80	–	–	–	–
6	120.20	120.40	120.50	120.70	120.80	120.9	–	–	–
7	120.20	120.40	120.50	120.70	120.80	120.9	120.9	–	–
8	120.20	120.40	120.50	120.70	120.70	120.80	120.80	120.90	–
9	120.20	120.30	120.40	120.70	120.70	120.80	120.80	120.90	120.90

From Table 5, the deviation of each sub-contour value from the row average is examined for the three- and nine-contour cases. For the three-contour case (average $J_C = 120.37$ GPa-Å), the deviation is observed to be minimum at 0.17 GPa-Å ($\approx 0.14\%$). For the nine-contour case (average $J_C = 120.63$ GPa-Å), deviation is observed to be maximum at 0.43 GPa-Å ($\approx 0.36\%$). In both cases, the deviations from the average remain well within an acceptable numerical tolerance, showing the path-independent nature of the computed J-integral.

From Figure 14, it is observed that beyond seven sub-contours, increasing the contour number further does not affect the result, i.e., the average J-integral converges at 120.63 GPa-Å for 7 sub-contours and beyond. For optimum computational efficiency, the seven sub-contour solution is therefore considered sufficient for subsequent analysis. As seven sub-contours, evaluated on the finest mesh, provide a stable average J-integral value, with negligible change under further contour extension, this outcome is therefore taken as the critical J-integral required for crack propagation in amorphous silica under the observed elastoplastic conditions. Accordingly, in the present work, the critical J-integral of amorphous silica is reported as

$$J_C^{\mathrm{FEM}} = 120.63 \text{ GPa-Å}. \tag{47}$$

This critical value, $J_C = 120.63$ GPa-Å, obtained using the finest mesh (22745 elements) and seven sub-contours, serves as the reference continuum result. With the reliability of this result confirmed, the following section compares the FEM predictions against the corresponding molecular dynamics (MD) results.

4 Results and Discussions

A direct comparison of fracture parameters obtained from different methodologies shows strong overall consistency between the atomistic observations and the elastoplastic continuum mechanics framework. The minor variations (shown in Table 6) observed are attributed to fundamental differences in the theoretical construction of each method, which are discussed in detail below.

Table 6: Critical fracture parameters for amorphous silica compared to $J_C^{\mathrm{MS}} = 119.9980$ GPa-Å

method	symbol	critical J_C (GPa-Å)	deviation from J_C^{MS}	deviation (%)
FE solution	J_C^{FEM}	120.63	$\frac{\lvert J_C^{\mathrm{FEM}} - J_C^{\mathrm{MS}}\rvert}{J_C^{\mathrm{MS}}}$	0.53
ERR (global energy)	G_C^{ERR}	113.74	$\frac{\lvert G_C^{\mathrm{ERR}} - J_C^{\mathrm{MS}}\rvert}{J_C^{\mathrm{MS}}}$	5.21
90° blunt tip CTOD	$G_C^{90^\circ}$	143.04	$\frac{\lvert G_C^{90^\circ} - J_C^{\mathrm{MS}}\rvert}{J_C^{\mathrm{MS}}}$	19.20
direct CTOD	G_C^{direct}	117.73	$\frac{\lvert G_C^{\mathrm{direct}} - J_C^{\mathrm{MS}}\rvert}{J_C^{\mathrm{MS}}}$	1.89

At the atomistic scale, the discretized loop-based J-integral calculation method provides the critical value of $J_C^{\mathrm{MS}} = 119.9980$ GPa-Å. This value is obtained by directly summing the strain energy density, stress, and displacement gradients at each atomistic site within the area integration domain (derived in Equation (31)). This formulation is treated as the primary molecular-scale fracture parameter in the present study, since it directly uses the mechanical deformation and stresses generated ahead of the crack tip, without relying on any theoretical model (such as the Ramberg-Osgood material model) or parametric assumption (e.g., the relation between CTOD and ERR). In contrast, the ERR and CTOD-based methods estimate the fracture parameter indirectly, through auxiliary relations involving global energy balance or yield strength. The discretized J-integral, by comparison, captures the near-tip elastoplastic fields explicitly and directly. While the present work establishes the critical J-integral of amorphous silica through an atomistic (and continuum elastoplastic) framework, it is instructive to place this value in the context of experimental and computational studies.

For amorphous silica specifically, an atomistic J-integral evaluated using an Irving-Kirkwood method reported a fracture toughness of $K_{IC} = 0.76 \pm 0.16$ MPa$\sqrt{\mathrm{m}}$ (Rimsza et al. (2018)). Using representative elastic constants for amorphous silica ($E = 75.26$ GPa, $\nu = 0.22$), this corresponds to a critical energy release rate of approximately $G_C \approx 73$ GPa-Å, which is substantially lower than the critical J-integral obtained in the present work. This underestimation relative to the present study may be attributed to the size of the inelastic process zone considered and the inherent applicability of LEFM; however, both values remain of the same order of magnitude, supporting the general validity of atomistic methods for calculating J-integral in amorphous silica.

A further atomistic scale comparison is available from a molecular dynamics study of surface-cracked amorphous silica (Chowdhury et al. (2019)), in which the J-integral had been computed as a function of applied far-field strain for several crack lengths using average atomic stresses over discretized regions. In this earlier study, the critical J-integral was reported to be independent of crack length for crack sizes of 3.0 nm and larger. The reported critical value, $J_C = 18.40 \pm 0.10$ J/m^2, corresponds to an apparent fracture surface energy of $\gamma \approx 9.20 \pm 0.05$ J/m^2. Converting this result to the units used in the present work (1 J/m^2 = 10 GPa-Å), the reported critical J-integral corresponds to $J_C = 184.0$ GPa $-$ Å. This value is substantially higher than the critical J-integral obtained in the present work from both atomistic ($J_C^{\mathrm{MS}} = 119.998$ GPa-Å). The authors of the earlier study note that their reported J_C is substantially larger than those of other studies they compared, attributing the excess to additional near-tip dissipation beyond simple bond rupture. This acknowledgment is consistent with the present understanding that the critical J-integral value includes contributions from near-tip inelastic or plastic-like dissipation.

An independent experimental measurement using Vickers indentation fracture toughness on glass (Gong (2002)) is also considered for comparison. Across a range of indentation loads from 4.9 N to 98 N, the reported indentation toughness (K_C) reaches a maximum value of $K_C = 0.978$ MPa$\sqrt{\mathrm{m}}$. Converting this to an equivalent critical energy release rate using $G_C = K_C^2(1-\nu^2)/E$, with $E = 75.26$ GPa and $\nu = 0.22$

(used in the present work taken from (Basu and Singh (2026))), gives

$$J_C^{\text{indent}} = \frac{K_C^2(1-\nu^2)}{E} \approx 120.9 \text{ GPa-Å}. \tag{48}$$

This value is in close agreement with the critical J-integral obtained in the present work, both from atomistic MD ($J_C^{\text{MD}} = 119.998$ GPa-Å) and from the continuum FEM analysis ($J_C^{\text{FEM}} = 120.63$ GPa-Å). It is important to note that indentation fracture is inherently governed by localized plastic deformation at the indent, which drives the radial cracks through the local elastoplastic stress field rather than through a purely elastic deformation at the corners of the indent (Gong (2002)). Since K_C is derived from the Vickers indentation method using the empirical relation between the indentation crack length, Young's modulus, hardening modulus, and stress intensity factor, it implicitly assumes an isotropic repose, which holds for amorphous silica. However, in practice, indentation itself implies that plastic deformation has occurred. Therefore, the critical J-integral may be explicitly formulated for this particular case. Since it is a more physically appropriate fracture parameter for comparison in this context than K_C itself. The close agreement observed here further supports the reliability of the critical J-integral computed for amorphous silica in the present work.

To intrinsically validate the obtained J-integral value, a global energy-based energy release rate (ERR) method is employed. This approach is computationally straightforward, as it does not require explicit discretization of near-tip atomistic sites or the evaluation of local-field quantities. The G_C^{MS} yields a slightly lower value (113.7407 GPa-Å), corresponding to an underprediction relative to the MS discrete loop method.

To establish a continuum-scale evaluation for comparison, the critical J-integral is independently evaluated using an elastoplastic finite element formulation. This continuum calculation yields a critical value of $J_C^{\text{FEM}} = 120.63$ GPa-Å, which is adopted as the benchmark FE reference in the present study, since it has been shown to converge with respect to both mesh refinement and the number of sub-contours. A notable outcome of this comparison is the excellent agreement between the continuum result, J_C^{FEM}, and the atomistic loop-based result, J_C^{MS}, with a deviation of approximately 0.53%. This close agreement stems directly from the similarity in how the J-integral is evaluated in the two frameworks. In both the molecular dynamics and finite element formulations, the J-integral is computed using a closed integration path, or its discrete-domain equivalent, that encloses the crack tip. This similar formulation ensures that the elastoplastic stress and displacement fields near the crack tip are captured consistently across length scales, allowing a direct comparison between the atomistic and continuum predictions.

Similarly, alternative methods for calculating ERR using CTOD have also been discussed. For clarity on the accuracy of each method, Table 6 summarizes the critical fracture parameters and their deviations relative to the atomistic J-integral value, J_C^{MS}.

As shown in Table 6, the 90° blunt-tip method for CTOD construction substantially overestimates the critical energy release rate for crack propagation initiation by

approximately 19%. This arises because the 90° blunt-tip method, by its geometric definition, overestimates the CTOD itself. For this reason, some researchers have proposed additional correction factors when calculating ERR from CTOD (Zhu et al. (2017); Nathan et al. (2021)). In the context of the present study, however, the 90° blunt-tip approach may be avoided in atomistic-scale fracture investigations, where accurate near-tip CTOD values can instead be obtained directly using the direct method.

The overall excellent agreement between J_C^{MS} and J_C^{FEM} further confirms the presence of elastoplastic deformation ahead of the crack tip, consistent with the agreement observed in the stress fields ahead of the crack tip between the two methods (Figure 7). This outcome also validates that the Ramberg-Osgood elastoplastic material constants, along with the yield strength, derived in the present work, can be reliably applied to fracture simulations.

The direct ERR and direct CTOD calculations are likewise accurate within a reasonable limit. The present study can therefore be used to determine the critical fracture parameters, either the J-integral or the ERR, at the onset of crack propagation. It is worth noting that both CTOD and ERR calculations are simpler and computationally less expensive than the discrete J-integral loop method. This makes them more practical for large sets of calculations, or for evaluating the ERR of a growing crack at successive timesteps, at the atomistic scale. Similarly, when CTOD itself needs to be evaluated, the direct method has been shown to yield accurate results and should therefore be the preferred approach.

5 Conclusions

This present work establishes a discretized, atomistic-scale J-integral formulation for amorphous silica and demonstrates its reliability through cross-validation with independent fracture parameters. To ensure robustness, the atomistic J-integral is compared with the energy release rate (ERR) derived from the global strain energy balance and the crack tip opening displacement (CTOD), computed using both a 90° blunt-tip method and a direct method. For continuum scale validation, an elastoplastic finite element analysis is performed using the Ramberg-Osgood elastoplastic model in the present study. The discretized J-integral was shown to be path-independent when a linear weight function is employed. It is shown that even if the integration domain encloses the near-tip inelastic zone, the present atomistic formulation retains the theoretical path-independence of the classical J-integral.

The critical atomistic J-integral J_C^{MS} is shown to be in excellent agreement with the continuum finite element result J_C^{FEM}. The global-energy ERR and the direct CTOD method also produced consistent estimates, further supporting the correctness of the discretization methodology. It has also been shown that the 90° blunt-tip CTOD method overestimated the critical energy release rate substantially, a consequence of its geometric construction to over-predict CTOD, and is therefore not recommended for atomistic-scale fracture analysis.

Taken together, these results confirm that linear elastic fracture mechanics is insufficient to describe crack propagation initiation in amorphous silica and that significant plastic deformation exists just ahead of the crack tip. Collectively, these results also

establish that the Ramberg-Osgood elastoplastic model can be reliably applied to capture this behavior at the continuum scale. This rigorously validated framework provides multiple methods for future elastoplastic fracture studies of amorphous silica, including extensions to varying crack geometries and orientations, loading directions and rates, and multiple crack interactions.

More generally, the discretized J-integral and finite element cross-validation framework developed in this work is not limited to amorphous silica. The methodology relies only on two material-specific input parameters. These are well-established interatomic potentials that accurately capture the mechanical response and near-tip stress distribution of the material of interest and the Ramberg-Osgood elastoplastic constants for use in the continuum finite element model. Given these two inputs are known, the present framework, comprising the atomistic loop-based J-integral, the global-energy ERR, the direct CTOD method, and the elastoplastic FEM benchmark, can be directly applied to replicate for any crystalline or amorphous elastoplastic material exhibiting near-tip plasticity, without requiring any additional modification to the formulation. This generality makes the present approach a versatile tool for evaluating elastoplastic fracture parameters across a wide range of material systems at the atomistic scale.

Acknowledgements. The authors acknowledge the IIT Delhi HPC facility for computational resources.

Declarations

- Funding: No funding was received for conducting this study or to assist with the preparation of this manuscript.
- Conflict of interest/Competing interests: The authors have no conflicts of interest to declare that are relevant to the content of this article.
- Data availability: The datasets generated and/or analyzed during the current study are available from the corresponding author on reasonable request.
- Code availability: The custom computational codes (LAMMPS, ABAQUS post-processing, and Python) are not publicly available due to ongoing research, but are available from the corresponding author on reasonable request.
- Author contribution: **Ayan Basu**: Conceptualization, Methodology, Computation, Data acquisition, Data visualization, Validation, Writing- Original Draft Preparation and Editing. **Gaurav Singh**: Conceptualization, Methodology, Data visualization, Supervision, Writing - Editing.

Appendix A Spatial derivatives of function $\boldsymbol{F}$ defined in Equation (26)

$$\begin{aligned}\frac{\partial F_j}{\partial X_j} &= \left(U\delta_{1j} - \sigma_{ij}u_{i,1}\right)\frac{\partial q}{\partial X_j} + q\left\{\frac{\partial}{\partial X_j}\left(U\delta_{1j} - \sigma_{ij}u_{i,1}\right)\right\} \\ &= \left(U\delta_{1j} - \sigma_{ij}u_{i,1}\right)\frac{\partial q}{\partial X_j} + q\left\{\frac{\partial U}{\partial X_1} - \frac{\partial \sigma_{ij}}{\partial X_j}\frac{\partial u_i}{\partial X_1} - \sigma_{ij}\frac{\partial u_i}{\partial X_1 \partial X_j}\right\}.\end{aligned} \tag{A1}$$

Now, as the body force is negligible with respect to the spatial derivatives of the Cauchy stress tensor, the equilibrium equation $\frac{\partial \sigma_{ij}}{\partial X_j} + b_i = 0$ gives $\frac{\partial \sigma_{ij}}{\partial X_j} = 0$. Thus, the expression can be shortened as

$$\frac{\partial F_j}{\partial X_j} = (U\delta_{1j} - \sigma_{ij} u_{i,1}) \frac{\partial q}{\partial X_j} + q \left\{ \frac{\partial U}{\partial X_1} - \sigma_{ij} \frac{\partial}{\partial X_1} \left(\frac{\partial u_i}{\partial X_j} \right) \right\}. \tag{A2}$$

For simplicity, the following is defined as

$$S_{ij} \overset{\text{def}}{=} \frac{\partial}{\partial X_1} \left(\frac{\partial u_i}{\partial X_j} \right) = \frac{\partial^2 u_i}{\partial X_1 \partial X_j}. \tag{A3}$$

The continuum definition of strain is defined as (Mase et al. (2020))

$$\varepsilon_{ij} = \frac{1}{2} \left(\frac{\partial u_i}{\partial X_j} + \frac{\partial u_j}{\partial X_i} \right). \tag{A4}$$

Taking the derivative of the above with respect to X_1 gives

$$\frac{\partial \varepsilon_{ij}}{\partial X_1} = \frac{1}{2} \left[\frac{\partial}{\partial X_1} \left(\frac{\partial u_i}{\partial X_j} \right) + \frac{\partial}{\partial X_1} \left(\frac{\partial u_j}{\partial X_i} \right) \right]. \tag{A5}$$

Applying the definition of S_{ij} shown in Equation (A3) the above equation can be written as

$$\frac{\partial \varepsilon_{ij}}{\partial X_1} = \frac{1}{2} \left[S_{ij} + S_{ji} \right]. \tag{A6}$$

So now, the last term of Equation (A2) can be written as

$$\sigma_{ij} \frac{\partial}{\partial X_1} \left(\frac{\partial u_i}{\partial X_j} \right) = \sigma_{ij} S_{ij} = \sigma_{ij} \frac{1}{2} (S_{ij} + S_{ij}) = \frac{1}{2} \sigma_{ij} S_{ij} + \frac{1}{2} \sigma_{ij} S_{ij}. \tag{A7}$$

Now, as both i and j are dummy indices summed over the same right-hand side itself, the indices can be swapped. So the above expression can be re-written as

$$\sigma_{ij} \frac{\partial}{\partial X_1} \left(\frac{\partial u_i}{\partial X_j} \right) = \frac{1}{2} (\sigma_{ij} S_{ij} + \sigma_{ji} S_{ji}). \tag{A8}$$

Now, it is known that the stress function is symmetric, i.e., $\sigma_{ij} = \sigma_{ji}$ (Mase et al. (2020)), the following can be written

$$\sigma_{ij} \frac{\partial}{\partial X_1} \left(\frac{\partial u_i}{\partial X_j} \right) = \frac{1}{2} (\sigma_{ij} S_{ij} + \sigma_{ij} S_{ji}) = \sigma_{ij} \frac{1}{2} (S_{ij} + S_{ji}). \tag{A9}$$

Finally, from the above expression and Equation (A6), the following can be written

$$\sigma_{ij} \frac{\partial}{\partial X_1} \left(\frac{\partial u_i}{\partial X_j} \right) = \sigma_{ij} \frac{\partial \varepsilon_{ij}}{\partial X_1}. \tag{A10}$$

Thus, Equation (A2) is now written as

$$\frac{\partial F_j}{\partial X_j} = \left(U\delta_{1j} - \sigma_{ij}u_{i,1}\right)\frac{\partial q}{\partial X_j} + q\left\{\frac{\partial U}{\partial X_1} - \sigma_{ij}\frac{\partial \varepsilon_{ij}}{\partial X_1}\right\}. \tag{A11}$$

Given U is the strain energy density function defined as $U = \frac{1}{2}\sigma_{ij}\varepsilon_{ij}$ (Mase et al. (2020)); and defined in the integral form as (shown in Equation (7))

$$U = \int_0^{\varepsilon} \sigma_{ij}\mathrm{d}\varepsilon_{ij} \tag{A12}$$

which, upon partial derivative, leads to

$$\partial U = \sigma_{ij}\partial\varepsilon_{ij} \tag{A13}$$

or

$$\frac{\partial U}{\partial \varepsilon_{ij}} = \sigma_{ij}. \tag{A14}$$

From a theoretical perspective, U is generally considered a function of strain only, leading to

$$U \equiv U(\varepsilon_{ij}) \equiv U[\varepsilon_{ij}(X_1, X_2)]. \tag{A15}$$

Therefore, taking the derivative with respect to X_1 gives

$$\frac{\partial U}{\partial X_1} = \frac{\partial U}{\partial \varepsilon_{ij}}\frac{\partial \varepsilon_{ij}}{\partial X_1}. \tag{A16}$$

Putting the expression derived in Equation (A14) in the above expression gives

$$\frac{\partial U}{\partial X_1} = \sigma_{ij}\frac{\partial \varepsilon_{ij}}{\partial X_1}. \tag{A17}$$

Therefore, Equation (A11) can now be written as

$$\frac{\partial F_j}{\partial X_j} = \left(U\delta_{1j} - \sigma_{ij}u_{i,1}\right)\frac{\partial q}{\partial X_j} + q\left\{\frac{\partial U}{\partial X_1} - \frac{\partial U}{\partial X_1}\right\} \tag{A18}$$

which finally leads to

$$\frac{\partial F_j}{\partial X_j} = \left(U\delta_{1j} - \sigma_{ij}u_{i,1}\right)\frac{\partial q}{\partial X_j}. \tag{A19}$$

Appendix B Calculation of the derivative of the weight function q

The weight function, as shown in Equation (24), can be written in terms of spatial coordinates as

$$q(r) \equiv q(X_1, X_2) = \frac{r - r_1}{r_2 - r_1} = \frac{\sqrt{X_1^2 + X_2^2} - r_1}{r_2 - r_1}. \tag{B20}$$

Partial differentiation of the above quantity with respect to X_j gives

$$\begin{aligned} \frac{\partial q}{\partial X_j} &= \begin{bmatrix} \frac{\partial q}{\partial X_1} \\ \frac{\partial q}{\partial X_2} \end{bmatrix} \\ &= \frac{1}{(r_2 - r_1)} \begin{bmatrix} \frac{X_1}{\sqrt{X_1^2 + x_2^2}} \\ \frac{X_2}{\sqrt{X_1^2 + x_2^2}} \end{bmatrix} \\ &= \frac{1}{r(r_2 - r_1)} \begin{bmatrix} X_1 \\ X_2 \end{bmatrix}. \end{aligned} \tag{B21}$$

Appendix C J-integral data tables for all inner radii (r_1)

Table C1: Discrete J-integral values and percentage deviation with respect to the first contour ($r_2 = 20$ Å) for $r_1 = 10$ Å.

r_1 (Å)	r_2 (Å)	No. of atoms in domain (N)	$r_2 - r_1$ (Å)	J (GPa-Å)	% deviation
10	20	794	10	103.3986	0.00
10	25	1463	15	103.5378	+0.14
10	30	2372	20	126.7141	+22.55
10	35	3361	25	115.5146	+11.71
10	40	4554	30	120.5101	+16.55
10	45	5935	35	113.2214	+9.50
10	50	7549	40	118.5983	+14.70
10	55	5293	45	122.6571	+18.62
10	60	11177	50	135.8009	+31.33
				$J_C = 117.7726$	

Table C2: Discrete J-integral values and percentage deviation with respect to the first contour ($r_2 = 25$ Å) for $r_1 = 15$ Å.

r_1 (Å)	r_2 (Å)	No. of atoms in domain (N)	$r_2 - r_1$ (Å)	J (GPa-Å)	% deviation
15	25	1139	10	131.7529	0.00
15	30	2048	15	120.3934	−8.62
15	35	3037	20	123.3591	−6.37
15	40	4230	25	115.1449	−12.61
15	45	5611	30	105.3039	−20.08
15	50	7225	35	118.9183	−9.74
15	55	8969	40	117.4005	−10.89
15	60	10853	45	127.2070	−3.45
15	65	13000	50	114.2767	−13.28
				$J_C = 119.3063$	

Table C3: Discrete J-integral values and percentage deviation with respect to the first contour ($r_2 = 35$ Å) for $r_1 = 25$ Å.

r_1 (Å)	r_2 (Å)	No. of atoms in domain (N)	$r_2 - r_1$ (Å)	J (GPa-Å)	% deviation
25	35	1898	10	125.8512	0.00
25	40	3091	15	132.8501	+5.56
25	45	4472	20	106.6018	−15.30
25	50	6068	25	117.4902	−6.64
25	55	7830	30	123.6756	−1.73
25	60	9714	35	110.1448	−12.48
25	65	11861	40	116.9369	−7.09
25	70	14002	45	130.4583	+3.66
25	75	16196	50	129.2016	+2.66
				$J_C = 121.4678$	

Table C4: Discrete J-integral values and percentage deviation with respect to the first contour ($r_2 = 40$ Å) for $r_1 = 30$ Å.

r_1 (Å)	r_2 (Å)	No. of atoms in domain (N)	$r_2 - r_1$ (Å)	J (GPa-Å)	% deviation
30	40	2182	10	110.5009	0.00
30	45	3563	15	110.1128	−0.35
30	50	5177	20	116.7879	+5.69
30	55	6921	25	131.9078	+19.37
30	60	8805	30	114.3655	+3.50
30	65	10952	35	131.6247	+19.12
30	70	13093	40	142.7538	+29.19
30	75	15287	45	126.1070	+14.12
30	80	17588	50	116.8809	+5.78
				$J_C = 122.3379$	

Table C5: Discrete J-integral values and percentage deviation with respect to the first contour ($r_2 = 45$ Å) for $r_1 = 35$ Å.

r_1 (Å)	r_2 (Å)	No. of atoms in domain (N)	$r_2 - r_1$ (Å)	J (GPa-Å)	% deviation
35	45	2574	10	110.9169	0.00
35	50	4188	15	111.4692	+0.50
35	55	5932	20	124.4816	+12.23
35	60	7816	25	133.6938	+20.54
35	65	9963	30	121.6042	+9.64
35	70	12104	35	133.4969	+20.36
35	75	12498	40	131.2418	+18.33
35	80	16599	45	111.6890	+0.70
35	85	18880	50	132.1401	+19.14
				$J_C = 123.4148$	

Table C6: Discrete J-integral values and percentage deviation with respect to the first contour ($r_2 = 50$ Å) for $r_1 = 40$ Å.

r_1 (Å)	r_2 (Å)	No. of atoms in domain (N)	$r_2 - r_1$ (Å)	J (GPa-Å)	% deviation
40	50	2995	10	130.5110	0.00
40	55	4739	15	127.4928	−2.31
40	60	6623	20	123.5239	−5.35
40	65	8770	25	112.5539	−13.74
40	70	10911	30	115.2054	−11.71
40	75	13105	35	112.9504	−13.45
40	80	15406	40	119.1654	−8.68
40	85	17687	45	111.4546	−14.59
40	90	19599	50	122.3083	−6.29
				$J_C = 119.4629$	

References

Anderson TL (2017) Fracture Mechanics: Fundamentals and Applications, 4th edn. CRC Press, https://doi.org/https://doi.org/10.1201/9781315370293

Aragones JL, Valeriani C, Vega C (2012) Note: Free energy calculations for atomic solids through the Einstein crystal/molecule methodology using GROMACS and LAMMPS. J Chem Phys 137(14):146101. https://doi.org/https://doi.org/10.1063/1.4758700

Bansal NP, Doremus RH (2013) Handbook of Glass Properties. Elsevier, Amsterdam, Netherlands

Basu A, Singh G (2024) Dependence of critical stress intensity factor on crack depth from the loading boundary of crystalline silicon. J Appl Mech 91:1–8. https://doi.

org/https://doi.org/10.1115/1.4064545

Basu A, Singh G (2026) Validity of plasticity in amorphous silica at small scale. Int J Solids Struct 339:114161. https://doi.org/https://doi.org/10.1016/j.ijsolstr.2026.114161

van Beest BWH, Kramer GJ, van Santen RA (1990) Force fields for silicas and aluminophosphates based on ab initio calculations. Phys Rev Lett 64(16):1955–1958. https://doi.org/https://doi.org/10.1103/PhysRevLett.64.1955

Bruns S, Petho L, Minnert C, et al (2020) Fracture toughness determination of fused silica by cube corner indentation cracking and pillar splitting. Mater Des 186:108311. https://doi.org/https://doi.org/10.1016/j.matdes.2019.108311

Chowdhury SC, Haque BZ, Gillespie JW (2016) Molecular dynamics simulations of the structure and mechanical properties of silica glass using ReaxFF. J Mater Sci 51(22):10139–10159. https://doi.org/https://doi.org/10.1007/s10853-016-0242-8

Chowdhury SC, Wise EA, Ganesh R, et al (2019) Effects of surface crack on the mechanical properties of silica: A molecular dynamics simulation study. Eng Fract Mech 207:99–108. https://doi.org/https://doi.org/10.1016/j.engfracmech.2018.12.025

Chu S, Liu C (2014) Finite element simulation of stable fatigue crack growth using critical CTOD determined by preliminary finite element analysis. Adv Mater Res 891–892:1675–1680. https://doi.org/https://doi.org/10.4028/www.scientific.net/AMR.891-892.1675

Cui P, Guo W (2020) Crack-tip-opening-displacement-based description of three-dimensional elastic-plastic crack border fields. Eng Fract Mech 231:107008. https://doi.org/https://doi.org/10.1016/j.engfracmech.2020.107008

van Duin ACT, Strachan A, Stewman S, et al (2003) $\mathrm{ReaxFF_{SiO}}$ reactive force field for silicon and silicon oxide systems. J Phys Chem A 107(19):3803–3811. https://doi.org/https://doi.org/10.1021/jp0276303

Dutta SK, Singh G (2024) Mechanics of crack initiation, propagation and crack grain boundary interaction in bicrystal silicon using near-tip localized stress calculation. Int J Solids Struct 296:112811. https://doi.org/https://doi.org/10.1016/j.ijsolstr.2024.112811

Dutta SK, Singh G (2025) Role of the distance between crack tip and grain boundary in mechanics of crack propagation in bicrystal silicon. Int J Solids Struct 313:113280. https://doi.org/https://doi.org/10.1016/j.ijsolstr.2025.113280

Evans DJ, Holian BL (1985) The Nose–Hoover thermostat. J Chem Phys 83(8):4069–4074. https://doi.org/https://doi.org/10.1063/1.449071

Gadamchetty G, Pandey A, Gawture M (2016) On practical implementation of the Ramberg-Osgood model for FE simulation. SAE Int J Mater Manuf 9:200–205. https://doi.org/https://doi.org/10.4271/2015-01-9086

Gong J (2002) Indentation toughness of ceramics: A statistical analysis. Ceram Int 28(7):767–772. https://doi.org/https://doi.org/10.1016/S0272-8842(02)00041-X

Gucci F, de Sousa Malafaia AM, Brighton J, et al (2025) Influence of notch geometry and temperature on the mechanical properties of Al-Mg alloy using molecular dynamics simulations. Fatigue Fract Eng Mater Struct 48(11):4769–4783. https://doi.org/https://doi.org/10.1111/ffe.70062

Gupta PK, Kurkjian CR (2005) Intrinsic failure and non-linear elastic behavior of glasses. J Non-Cryst Solids 351(27-29):2324–2328. https://doi.org/https://doi.org/10.1016/j.jnoncrysol.2005.05.029

Gupta RP (1985) Electronic structure of crystalline and amorphous silicon dioxide. Phys Rev B 32(12):8278–8292. https://doi.org/https://doi.org/10.1103/PhysRevB.32.8278

Gurtin ME, Fried E, Anand L (2013) The Mechanics and Thermodynamics of Continua. Cambridge University Press, Cambridge

Han SM, Xie C, Cui Y (2010) Microcompression of fused silica nanopillars synthesized using reactive ion etching. Nanosci Nanotechnol Lett 2:344–347. https://doi.org/https://doi.org/10.1166/nnl.2010.1105

Hao T, Hossain ZM (2019) Atomistic mechanisms of crack nucleation and propagation in amorphous silica. Phys Rev B 100:1–18. https://doi.org/https://doi.org/10.1103/PhysRevB.100.014204

Hatty V, Kahn H, Heuer AH (2008) Fracture toughness, fracture strength, and stress corrosion cracking of silicon dioxide thin films. J Microelectromech Syst 17(4):943–947. https://doi.org/https://doi.org/10.1109/JMEMS.2008.927069

Horstemeyer MF, Baskes MI (1999) Atomistic finite deformation simulations: A discussion on length scale effects in relation to mechanical stresses. J Eng Mater Technol 121:114–119. https://doi.org/https://doi.org/10.1115/1.2812354

Huff NT, Demiralp E, Çagin T, et al (1999) Factors affecting molecular dynamics simulated vitreous silica structures. J Non-Cryst Solids 253:133–142. https://doi.org/https://doi.org/10.1016/S0022-3093(99)00349-X

Jia P, Huang K, Yu H, et al (2022) A novel atomic J-integral concept beyond conventional fracture mechanics. Theor Appl Fract Mech 121:103531. https://doi.org/https://doi.org/10.1016/j.tafmec.2022.103531

Jones RE, Rimsza JM, Criscenti LJ (2018) An atomic-scale evaluation of the fracture toughness of silica glass. J Phys Condens Matter 30:245901. https://doi.org/https://doi.org/10.1088/1361-648X/aac28b

Kermouche G, Guillonneau G, Michler J, et al (2016) Perfectly plastic flow in silica glass. Acta Mater 114:146–153. https://doi.org/https://doi.org/10.1016/j.actamat.2016.05.027

Khan D, Biswas K (2010) On the evaluation of path independent integral J_F^* for circular arc crack. Mech Based Des Struct Mach 38(3):300–327. https://doi.org/https://doi.org/10.1080/15397731003727103

Khare R, Mielke SL, Paci JT, et al (2007) Coupled quantum mechanical / molecular mechanical modeling of the fracture of defective carbon nanotubes and graphene sheets. Phys Rev B 75:075412. https://doi.org/https://doi.org/10.1103/PhysRevB.75.075412

Ktari A, Baccar M, Shah M, et al (2014) A crack propagation criterion based on ΔCTOD measured with 2D-digital image correlation technique. Fatigue Fract Eng Mater Struct 37:682–694. https://doi.org/https://doi.org/10.1111/ffe.12153

Landes JD, Begley JA, Clarke GA (1979) Elastic-Plastic Fracture. ASTM Special Technical Publication, American Society for Testing and Materials, Philadelphia, PA

Liu W, Huang H, Chen Z, et al (2011) Simulation of crack tip plasticity using 3D crystal plasticity theory. Adv Mater Res 294:1057–1061. https://doi.org/https://doi.org/10.4028/www.scientific.net/AMR.291-294.1057

Liu Z (2024) Quantitative predictive theories through integrating quantum, statistical, equilibrium, and nonequilibrium thermodynamics. J Phys Condens Matter 36(34):343003. https://doi.org/https://doi.org/10.1088/1361-648X/ad4762

Lu Q, Gao W, Huang R (2011) Atomistic simulation and continuum modeling of graphene nanoribbons under uniaxial tension. Modell Simul Mater Sci Eng 19:054006. https://doi.org/https://doi.org/10.1088/0965-0393/19/5/054006

Lubliner J (2008) Plasticity Theory, revised edn. Dover Publications, New York

Mantisi B, Tanguy A, Kermouche G, et al (2012) Atomistic response of a model silica glass under shear and pressure. Eur Phys J B 85:304. https://doi.org/https://doi.org/10.1140/epjb/e2012-30317-6

Marsh DM (1964) Plastic flow in glass. Proc R Soc Lond A 279(1378):420–435. https://doi.org/https://doi.org/10.1098/rspa.1964.0114

Mase GT, Smelser RE, Rossmann JS (2020) Continuum Mechanics for Engineers, 4th edn. CRC Press, Boca Raton

Metzger M, Seifert T, Schweizer C (2015) Does the cyclic J-integral ΔJ describe the crack-tip opening displacement in the presence of crack closure? Eng Fract Mech 134:459–473. https://doi.org/https://doi.org/10.1016/j.engfracmech.2014.07.017

Munetoh S, Motooka T, Moriguchi K, et al (2007) Interatomic potential for Si–O systems using Tersoff parameterization. Comput Mater Sci 39(2):334–339. https://doi.org/https://doi.org/10.1016/j.commatsci.2006.06.010

Muralidharan K, Simmons JH, Deymier PA, et al (2005) Molecular dynamics studies of brittle fracture in vitreous silica: Review and recent progress. J Non-Cryst Solids 351:1532–1542. https://doi.org/https://doi.org/10.1016/j.jnoncrysol.2005.03.026

Muralidharan K, Mallik A, Runge K, et al (2006) Implementation of consistent embedding for a larger system–amorphous silica. J Comput Aided Mater Des 13(1–3):61–73. https://doi.org/https://doi.org/10.1007/s10820-006-9015-z

Muralidharan K, Oh KD, Deymier PA, et al (2007) Molecular dynamics simulations of atomic-level brittle fracture mechanisms in amorphous silica. J Mater Sci 42(12):4159–4169. https://doi.org/https://doi.org/10.1007/s10853-007-1638-2

Nathan M, Hertelé S, Sarzosa DFB (2021) On the experimental estimation of CTOD fracture parameter using SE(T) specimens based upon only one clip gauge measurement. Eng Fract Mech 253:107856. https://doi.org/https://doi.org/10.1016/j.engfracmech.2021.107856

Nikishkov GP, Vershinin AV, Nikishkov YG (2016) Mesh-independent equivalent domain integral method for J-integral evaluation. Adv Eng Softw 100:308–318. https://doi.org/https://doi.org/10.1016/j.advengsoft.2016.08.006

Okada H, Ohata S (2013) Three-dimensional J-integral evaluation for cracks with arbitrary curvatures and kinks based on domain integral method for quadratic tetrahedral finite element. Eng Fract Mech 109:58–77. https://doi.org/https://doi.org/10.1016/j.engfracmech.2013.06.009

Parks DM (1977) A stiffness derivative finite element technique for determination of crack tip stress intensity factors. Int J Fract 10(4):487–502. https://doi.org/https://doi.org/10.1007/BF00155252

Patwardhan PS, Nalavde RA, Kujawski D (2019) An estimation of Ramberg-Osgood constants for materials with and without Luder's strain using yield and ultimate strengths. Procedia Struct Integrity 17:750–757. https://doi.org/https://doi.org/10.1016/j.prostr.2019.08.100

Pedone A, Malavasi G, Menziani MC, et al (2008) Molecular dynamics studies of stress-strain behavior of silica glass under a tensile load. Chem Mater 20(13):4356–4366. https://doi.org/https://doi.org/10.1021/cm800413v

Ramachandramoorthy R, Schwiedrzik J, Petho L, et al (2019) Dynamic plasticity and failure of microscale glass: Rate-dependent ductile-brittle-ductile transition. Nano Lett 19:2350–2359. https://doi.org/https://doi.org/10.1021/acs.nanolett.8b05024

Ramberg W, Osgood WR (1943) Description of stress-strain curves by three parameters. Tech. Rep. Technical Note No. 902, National Advisory Committee for Aeronautics, Washington, D.C.

Rice JR, Rosengren GF (1968) Plane strain deformation near a crack tip in a power-law hardening material. J Mech Phys Solids 16(1):1–12. https://doi.org/https://doi.org/10.1016/0022-5096(68)90013-6

Rimsza JM, Jones RE, Criscenti LJ (2018) Crack propagation in silica from reactive classical molecular dynamics simulations. J Am Ceram Soc 101:1488–1499. https://doi.org/https://doi.org/10.1111/jace.15292

Robertson J (2006) Electronic structure of amorphous silicon dioxide. Rep Prog Phys 69:327–396. https://doi.org/https://doi.org/10.1088/0034-4885/69/2/R02

Roy S, Roy A (2019) A computational investigation of length-scale effects in the fracture behaviour of a graphene sheet using the atomistic J-integral. Eng Fract Mech 207:165–180. https://doi.org/https://doi.org/10.1016/j.engfracmech.2018.12.012

Samadian K, Hertelé S, De Waele W (2018) Using 3D digital image correlation (3D-DIC) to measure CTOD in a semi-elliptical surface crack. Proceedings 2(8):451. https://doi.org/https://doi.org/10.3390/ICEM18-05311

Schill W, Heyden S, Conti S, et al (2018) The anomalous yield behavior of fused silica glass. J Mech Phys Solids 113:105–125. https://doi.org/https://doi.org/10.1016/j.jmps.2018.01.004

Shih CF, Moran B, Nakamura T (1986) Energy release rate along a three-dimensional crack front in a thermally stressed body. Int J Fract 30(2):79–102. https://doi.org/https://doi.org/10.1007/BF00034019

Silva ECCM, Tong L, Yip S, et al (2006) Size effects on the stiffness of silica nanowires. Small 2:239–243. https://doi.org/https://doi.org/10.1002/smll.200500311

Singh A, Singh G (2023) A localized near crack tip stress field approach for calculating the fracture strength of an anisotropic solid at an atomistic scale. Mech Mater 181:104632. https://doi.org/https://doi.org/10.1016/j.mechmat.2023.104632

Singh G, Kermode JR, De Vita A, et al (2014) Validity of linear elasticity in the crack-tip region of ideal brittle solids. Int J Fract 189:103–110. https://doi.org/https://doi.org/10.1007/s10704-014-9958-0

Skogsrud J, Thaulow C (2015) Application of CTOD in atomistic modeling of fracture. Eng Fract Mech 150:153–160. https://doi.org/https://doi.org/10.1016/j.engfracmech.2015.08.043

Smith M (2009) ABAQUS/Standard User's Manual, Version 6.9. Dassault Systèmes Simulia Corp., United States

Sohail T, Roy S (2023) An investigation of the validity of LEFM at the nanoscale in amorphous materials using the atomistic J-integral including entropic effect. Theor Appl Fract Mech 125:103913. https://doi.org/https://doi.org/10.1016/j.tafmec.2023.103913

Stenström C, Eriksson K (2021) The J-area integral applied in peridynamics. Int J Fract 228(2):127–142. https://doi.org/https://doi.org/10.1007/s10704-020-00505-8

Stukowski A (2009) Visualization and analysis of atomistic simulation data with OVITO – the Open Visualization Tool. Modell Simul Mater Sci Eng 18:015012. https://doi.org/https://doi.org/10.1088/0965-0393/18/1/015012

Swadener JG, Baskes MI, Nastasi M (2002) Molecular dynamics simulation of brittle fracture in silicon. Phys Rev Lett 89(8):085503. https://doi.org/https://doi.org/10.1103/PhysRevLett.89.085503

Thompson AP, Aktulga HM, Berger R, et al (2022) LAMMPS — a flexible simulation tool for particle-based materials modeling at the atomic, meso, and continuum scales. Comput Phys Commun 271:108171. https://doi.org/https://doi.org/10.1016/j.cpc.2021.108171

Vashishta P, Kalia RK, Rino JP, et al (1990) Interaction potential for SiO_2: A molecular-dynamics study of structural correlations. Phys Rev B 41(17):12197–12209. https://doi.org/https://doi.org/10.1103/PhysRevB.41.12197

Velilla-díaz W, Ricardo L, Palencia A (2021) Fracture toughness estimation of single-crystal aluminum at nanoscale. Nanomaterials 11(3):680. https://doi.org/https://doi.org/10.3390/nano11030680

Wang J, Rajendran AM, Dongare AM (2015) Atomic scale modeling of shock response of fused silica and α-quartz. J Mater Sci 50:8128–8141. https://doi.org/https://doi.org/10.1007/s10853-015-9386-1

Watanabe M (2020) Extension of Inglis's elliptic crack solution. Theor Appl Fract Mech 109:102756. https://doi.org/https://doi.org/10.1016/j.tafmec.2020.102756

Widmer RN, Groetsch A, Kermouche G, et al (2022) Temperature–dependent dynamic plasticity of micro-scale fused silica. Mater Des 215:110503. https://doi.org/https://doi.org/10.1016/j.matdes.2022.110503

Wiederhorn SM (1969) Fracture surface energy of glass. J Am Ceram Soc 52(2):99–105. https://doi.org/https://doi.org/10.1111/j.1151-2916.1969.tb13350.x

Xu GQ, Demkowicz MJ (2020) Computing critical energy release rates for fracture in atomistic simulations. Comput Mater Sci 181:109738. https://doi.org/https://doi.org/10.1016/j.commatsci.2020.109738

Yuan F, Huang L (2012) Molecular dynamics simulation of amorphous silica under uniaxial tension: From bulk to nanowire. J Non-Cryst Solids 358:3481–3487. https://doi.org/https://doi.org/10.1016/j.jnoncrysol.2012.05.045

Yuan F, Huang L (2014) Brittle to ductile transition in densified silica glass. Sci Rep 4:5035. https://doi.org/https://doi.org/10.1038/srep05035

Yue Y, Zheng K (2014) Strong strain rate effect on the plasticity of amorphous silica nanowires. Appl Phys Lett 104:231906. https://doi.org/https://doi.org/10.1063/1.4882420

Zhang K, Tian T, Li Y, et al (2025) Path-independent axisymmetric J-integral for the chemo-mechanical fracture analysis of elastoplastic electrodes in lithium-ion batteries. Int J Solids Struct 313:113291. https://doi.org/https://doi.org/10.1016/j.ijsolstr.2025.113291

Zhang Z, Wang X, Lee JD (2014) An atomistic methodology of energy release rate for graphene at nanoscale. J Appl Phys 115(11):114314. https://doi.org/https://doi.org/10.1063/1.4869207

Zhu T, Li J, Yip S, et al (2003) Deformation and fracture of a SiO_2 nanorod. Mol Simul 29(10–11):671–676. https://doi.org/https://doi.org/10.1080/0892702031000103220

Zhu X, Zelenak P, McGaughy T (2017) Comparative study of CTOD-resistance curve test methods for SENT specimens. Eng Fract Mech 172:17–38. https://doi.org/https://doi.org/10.1016/j.engfracmech.2017.01.007